

Geospatial Immune Heterogeneity Reflects the Diverse Tumor–Immune Interactions in Intrahepatic Cholangiocarcinoma



Youpei Lin¹, Lihua Peng^{2,3}, Liangqing Dong¹, Dongbing Liu^{2,3}, Jiaqiang Ma¹, Jian Lin¹, Xiaofang Chen^{2,3}, Penghui Lin^{2,3}, Guohe Song¹, Mao Zhang¹, Yuming Liu¹, Junhua Rao², Chen Wei^{2,4}, Ye Lu^{2,4}, Shu Zhang¹, Guangyu Ding¹, Zhenyu Peng⁵, Haorong Lu⁵, Xiaoying Wang¹, Jian Zhou^{1,6}, Jia Fan^{1,6}, Kui Wu^{2,3}, and Qiang Gao^{1,6,7}

ABSTRACT

Intrahepatic cholangiocarcinoma (iCCA) exhibits extensive intratumoral heterogeneity and an extremely high mortality rate. Here, we performed whole-exome sequencing, RNA sequencing, T-cell receptor (TCR) sequencing, and multiplexed immunofluorescence on 207 tumor regions from 45 patients with iCCA. Over half of iCCA displayed intratumoral heterogeneity of immune infiltration, and iCCA were classified into sparsely, heterogeneously, and highly infiltrated subgroups with distinct immunogenomic characteristics. Sparsely infiltrated tumors displayed active copy-number loss of clonal neoantigens, and heterogeneous immune infiltration played an important role in the subclonal evolution across tumor subregions. Highly infiltrated tumors were characterized by extensive immune activation and a similar TCR repertoire across tumor subregions, but counteracted with T-cell exhaustion and pervasive antigen presentation defects. Notably, *FGFR2* mutations and fusions correlated with low mutation burden and reduced immune infiltration. Our work delineated the dynamic tumor–immune interactions and developed a robust classification system to divide patients with iCCA into high and low immune evasion groups with different prognoses.

SIGNIFICANCE: This study elucidates the impact of spatial immune heterogeneity upon tumor evolution of iCCA and reveals distinct immune evasion mechanisms developed in different immune microenvironments, which can be exploited for the development of personalized immunotherapy strategies.

¹Department of Liver Surgery and Transplantation, Liver Cancer Institute, Zhongshan Hospital, and Key Laboratory of Carcinogenesis and Cancer Invasion (Ministry of Education), Fudan University, Shanghai, China. ²BGI-Shenzhen, Beishan Industrial Zone, Shenzhen, China. ³Guangdong Provincial Key Laboratory of Human Disease Genomics, Shenzhen Key Laboratory of Genomics, Shenzhen, China. ⁴College of Life Sciences, University of Chinese Academy of Sciences, Beijing, China. ⁵China National GeneBank, BGI-Shenzhen, Shenzhen, China. ⁶Key Laboratory of Medical Epigenetics and Metabolism, Institutes of Biomedical Sciences, Fudan University, Shanghai, China. ⁷State Key Laboratory of Genetic Engineering, Fudan University, Shanghai, China.

Note: Y. Lin, L. Peng, L. Dong, and D. Liu contributed equally to this article.

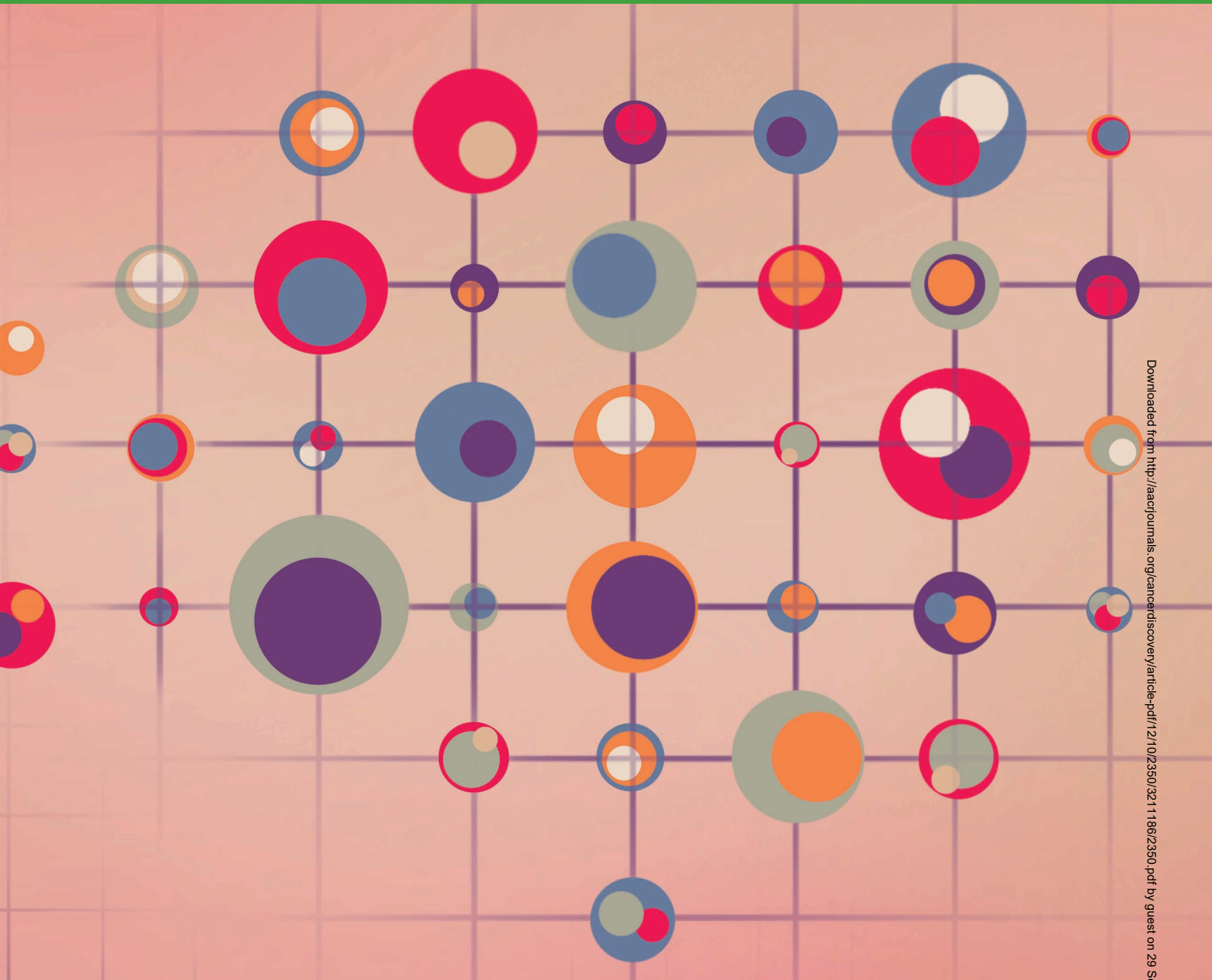
Corresponding Authors: Qiang Gao, Department of Liver Surgery and Transplantation, Liver Cancer Institute, Zhongshan Hospital, Fudan University,

180 Fenglin Road, Shanghai 200032, China. Phone: 86-21-6403-7181; E-mail: gaoqiang@fudan.edu.cn; Kui Wu, BGI-Shenzhen, Beishan Industrial Zone, Shenzhen 518083, China. Phone: 86-755-3394-5599; E-mail: wukui@genomics.cn; and Jia Fan, Department of Liver Surgery and Transplantation, Liver Cancer Institute, Zhongshan Hospital, Fudan University, 180 Fenglin Road, Shanghai 200032, China. Phone: 86-21-6404-1990; E-mail: fan.jia@zs-hospital.sh.cn

Cancer Discov 2022;12:2350–71

doi: 10.1158/2159-8290.CD-21-1640

©2022 American Association for Cancer Research



INTRODUCTION

Intrahepatic cholangiocarcinoma (iCCA) is the second most common primary liver cancer, with increasing incidence worldwide (1). Characterized by high invasiveness and frequent postoperative recurrence, iCCA exhibits one of the highest mortality rates among human cancers. Despite the recent progress with novel therapies targeting *IDH1* mutation (2) and *FGFR2* fusion (3–5), iCCA is still incurable in most cases. Immune-checkpoint inhibitors (ICI) have revolutionized the standard treatment for patients with cancer, but the objective response rates range from only 3% to 22% in biliary cancers (6). One major challenge is the poor understanding of the tumor–immune interaction in iCCA, which impedes the identification of patients for effective immunotherapy.

The tumor–immune interaction is a dynamic and continuous process. Infiltrated immune cells hold the potential of killing malignant cells, representing the major external selection pressure to orchestrate tumor evolution (7). We have previously illustrated the spatiotemporal genomic evolution of iCCA through multiregion sampling–derived cancer cell cultures, linking with drug resistance, but we did not focus on the immune microenvironment (8). Single-cell RNA sequencing (RNA-seq) analyses have emphasized the impact of transcriptomic diversity of cancer cells on patient survival and treatment response in iCCA (9, 10). Accumulating studies have uncovered the effect of the tumor–immune interaction on tumor progression, drug resistance, and immune tolerance in many other cancers (11–13). Likewise, a recent study has

also characterized the high intratumoral heterogeneity (ITH) and “cold” tumor microenvironment in patients with *IDH*-mutant iCCA (14). An in-depth exploration of such a relationship in iCCA may have the promise to enable more precise development for targeted therapy and immunotherapy (15).

Herein, we collected 207 tumor samples from 45 patients with treatment-naïve iCCA and performed whole-exome sequencing (WES), transcriptome sequencing, T-cell receptor sequencing (TCR-seq), and multiplex staining to portray the immunogenomic landscape of iCCA. Our results demonstrate the diversity of immune infiltration in iCCA, and those with sparse, heterogeneous, or high immune infiltration have different genetic characteristics and escape mechanisms. The integration of immunogenomic analyses provides a novel insight into how iCCA's genetic makeup affects immune composition and function and vice versa.

RESULTS

Early Branch Evolution and Potential Therapeutic Targets in iCCA

To elucidate the immunogenomic landscape of iCCA, we prospectively assembled 207 tumor samples, together with paired nontumor liver tissues and peripheral blood, from 45 patients (four to six tumor regions per patient), and performed high-depth WES, RNA-seq, TCR-seq, and multiplex immunofluorescence (Supplementary Fig. S1A and S1B; Supplementary Table S1). None of the patients had received preoperative anticancer treatments. Two tumor samples were excluded for further analysis due to low tumor purity (<0.1). The average depth of WES was 284.7× for tumor samples (range, 196.5–584.7) and 247.5× for normal controls (range, 150.8–527.9), respectively. In total, we identified 30,348 somatic mutations (range, 47–509, averaging 148 per tumor sample), including 27,749 (91.4%) point mutations and 2,599 (8.6%) indels (Supplementary Table S1).

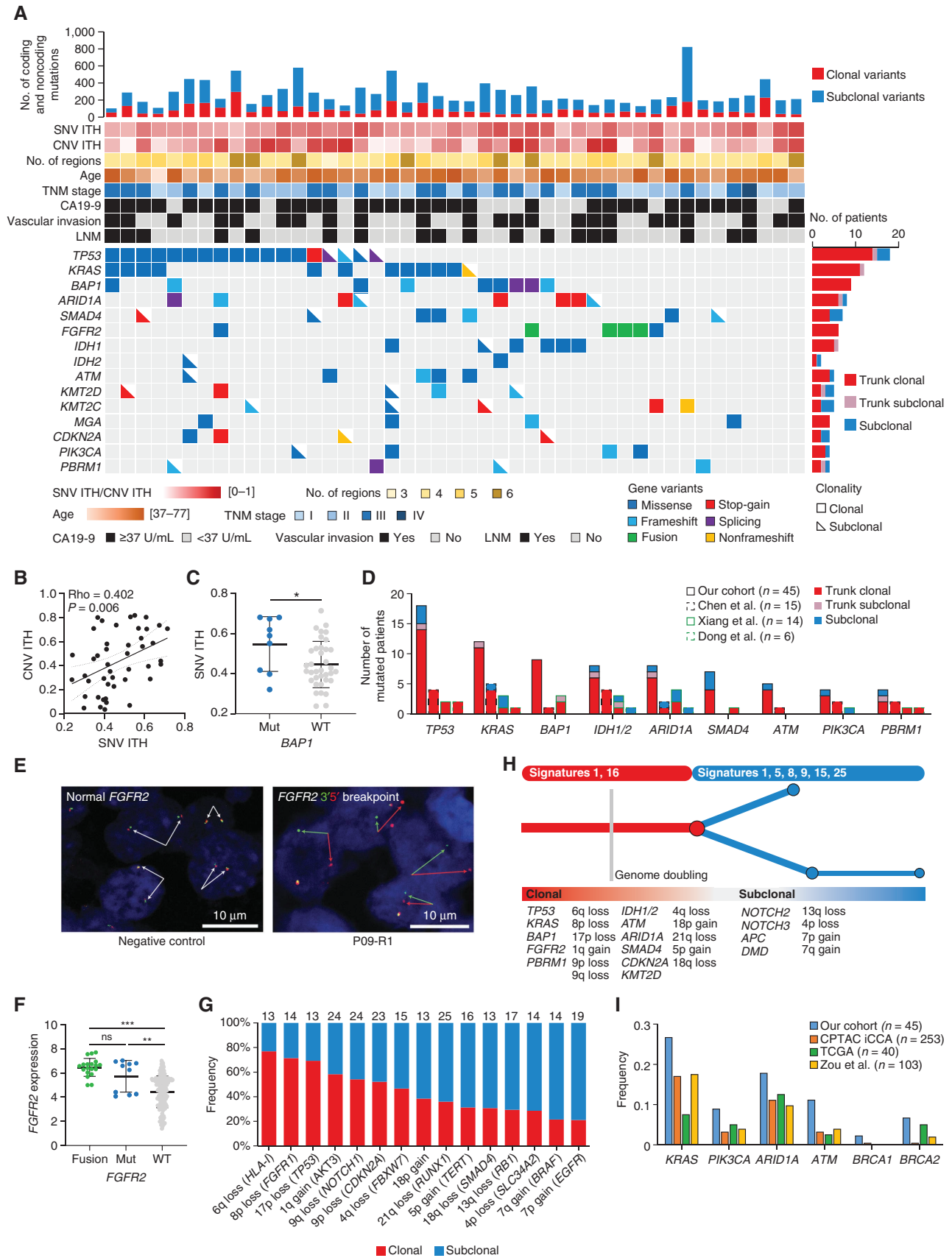
We observed considerable intratumoral genomic heterogeneity, with a median of 65.1% (range, 43.6%–89.3%) of single-nucleotide variations (SNV) and 66.0% (range, 9.1%–100%) of copy-number variations (CNV) identified as subclonal (Fig. 1A). The median pairwise SNV ITH and CNV ITH were 42.8% (range, 23.8%–71.4%) and 41.1% (range, 3.6%–81.8%), respectively, suggesting that over 40% of the SNVs and CNVs were distinct among tumor subregions within the same patients (Fig. 1A; Supplementary Table S1). There was a moderately positive correlation between SNV ITH and CNV ITH (Spearman correlation = 0.402, $P = 0.006$), indicating that tumor evolution coexisted at the mutational and chromosomal levels (Fig. 1B). Loss-of-function mutations in *BAP1* can damage genomic stability and DNA repair (16), and iCCA patients with *BAP1* mutations showed significantly higher levels of SNV ITH (Fig. 1C).

We identified a total of 510 driver mutations (range, 4–30 per patient, averaging 11.4), of which 237 (46.5%) were clonal and 273 (53.5%) were subclonal. We further investigated the timing of recurrent driver mutations by integrating three recent multiregion sampling studies of iCCA (refs. 8, 14, 17; Fig. 1D; Supplementary Fig. S1C). Generally, *TP53*, *KRAS*, *BAP1*, and *PBRM1* mutations were clonal, highlighting their essential roles in tumorigenesis. *IDH1/2*, *ARID1A*, *SMAD4*, *ATM*, and *PIK3CA* mutations were primarily clonal but also subclonal in some patients, implying their dual roles in driving tumorigenesis and progression. We found that subclonal driver mutations could also induce pathway alterations of tumor cells in corresponding subregions (Supplementary Fig. S2). For example, P41-R3 with *ARID1A* mutation displayed downregulated DNA double-strand break repair compared with other subregions in P41, consistent with *ARID1A*'s role in mismatch repair (18).

FGFR2 fusions were identified in four patients of our cohort, with the same breaking point but different partner genes (Supplementary Fig. S3A). The occurrence of the *FGFR2* fusion was validated in all tumor subregions and nearly all tumor cells using Sanger sequencing and fluorescent *in situ* hybridization (FISH), respectively, suggesting that it occurred early during tumor evolution (Fig. 1E; Supplementary Fig. S3A). Meanwhile, clonal *FGFR2* mutations were detected in another two patients, and the six cases with *FGFR2* alterations exhibited significantly higher expression of *FGFR2* than wild-type (Fig. 1F). We also obtained multiomics data from the Clinical Proteomic Tumor Analysis Consortium (CPTAC) iCCA cohort ($n = 249$; ref. 19) and analyzed the CNV of *FGFR2*. The frequency of *FGFR2* loss was similar between our cohort and the CPTAC cohort (15.6% vs. 13.7%), whereas a lower frequency of *FGFR2* gain was observed in ours (8.3% vs. 17.3%; Supplementary Fig. S3B). Focal *FGFR2* amplification was only found in one patient in our cohort, co-occurred with *FGFR2* fusion, and existed in all tumor subregions on FISH images (Supplementary Fig. S3C). There was no significant difference in *FGFR2* expression between samples with *FGFR2* copy-number neutral and gain in both cohorts, in contrast to its mutation/fusion-induced higher expression (Supplementary Fig. S3D).

Chromosome 6q loss (where HLA class I molecules are located) occurred early, implying an immediate decline of antigen presentation after tumor initiation (Fig. 1G). Loss of *TP53* (17p) and *CDKN2A* (9p) was also an early event, whereas gain of *EGFR* (7p) and *BRAF* (7q) was a late event. We then analyzed mutation signatures and found different distribution between clonal and subclonal mutations (Supplementary Fig. S3E). Signature 16 (special signature in liver cancer) and signature 1 (spontaneous deamination of 5-methylcytosine correlating with age) were dominant in clonal mutations, whereas the signatures of subclonal mutations were more diverse, including signatures 1, 5, 8, 9, 15, and 25. Taken together, iCCA showed

Figure 1. Clonal architecture and therapeutic targets of iCCA. **A**, Timing of genetic profile and associated clinicopathologic characteristics. LNM, lymph node metastasis. **B**, Correlation of SNV ITH and CNV ITH; Spearman test. TNM, tumor-node-metastasis. **C**, Comparison of SNV ITH between patients with and without *BAP1* mutations; Student t test. The mean and the first and third quartiles are indicated by the thick horizontal line and whiskers of the scatter plot, respectively. *, $P < 0.05$; **, $P < 0.01$; ***, $P < 0.001$; ns, not significant. Mut, mutation; WT, wild-type. **D**, Timing of recurrent driver mutations in four multiregion sampling studies of iCCA. **E**, *FGFR2* fusion validated by FISH in P09-R1. The green and red fluorescent probes target the proximal end (3') and distal end (5') of the *FGFR2* gene, respectively. **F**, Comparison of *FGFR2* expression among tumor samples with *FGFR2* fusions, *FGFR2* mutations, and WT; Student t test. **G**, Clonality of chromosome arm copy-number alterations. The numbers on the top represent actual patient numbers with copy-number alterations. **H**, The illustration of clonal evolution trajectory of iCCA. **I**, Mutation frequencies of indicated mutations in four iCCA cohorts. TCGA, The Cancer Genome Atlas.



Downloaded from <http://aacrjournals.org/cancerdiscovery/article-pdf/12/10/2350/321186/2350.pdf> by guest on 29 September 2023

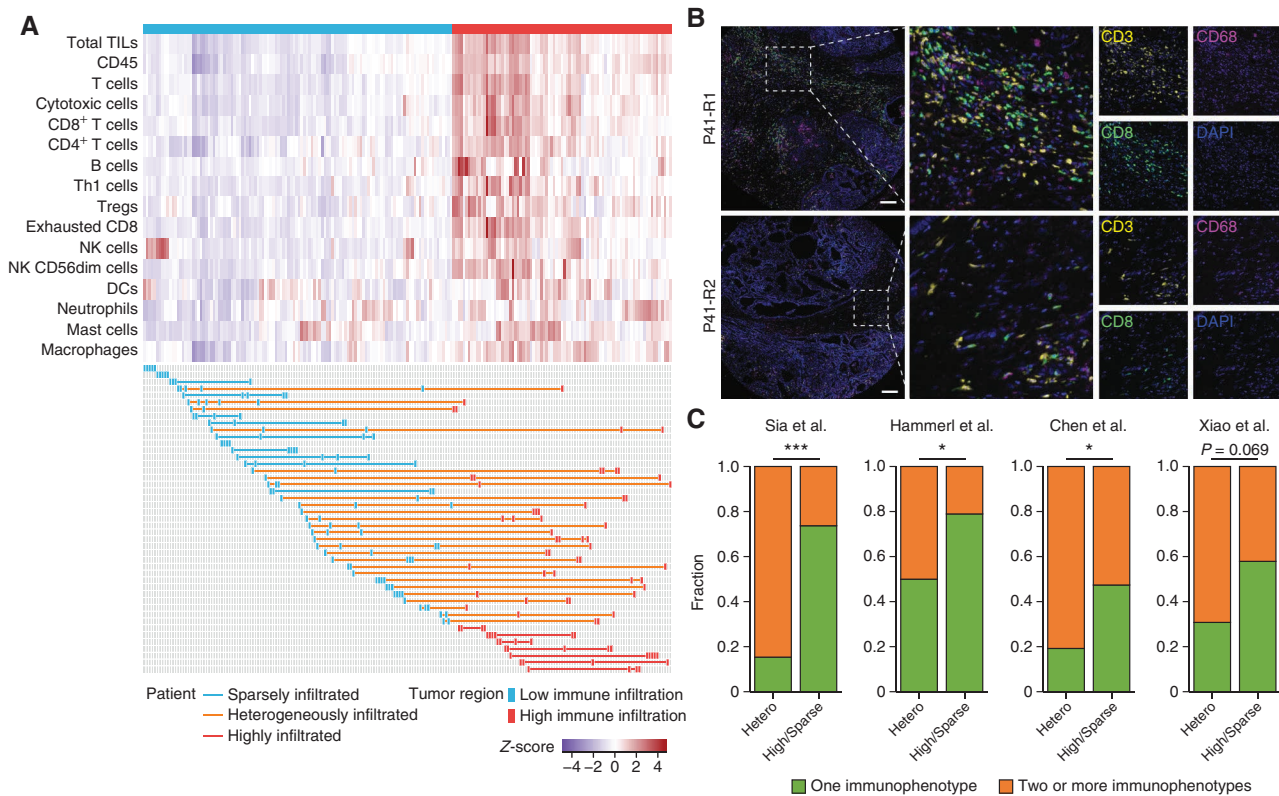


Figure 2. Heterogeneity of immune infiltration in iCCA. **A**, Hierarchical clustering of immune infiltration across iCCA samples ($n = 205$). Each row represents an indicated immune cell, and each column represents a tumor region. Tumor regions are classified as low (blue) and high (red) immune infiltration on the top. Blue, orange, and red lines on the bottom represent patients with uniformly low, heterogeneous, and uniformly high immune infiltration, respectively. DC, dendritic cell; NK, natural killer; Treg, regulatory T cell. **B**, Representative immunostaining images showing the ITH of immune infiltration in P41: CD3 (yellow), CD68 (purple), CD8 (green), and DAPI (blue). Scale bars, 200 μm . **C**, Immune diversity of tumor subregions in different groups as defined by the four transcriptome-based immunophenotypic classifiers. Tumors with all subregions displaying one immunophenotype are shown in green; otherwise, they are shown in orange. (continued on following page)

evolutionary branches at the early stage, with both driver gene alterations (*TP53*, *KRAS*, *BAP1*, *FGFR2*, *PBRM1*) and CNVs (6q loss, 8p loss, 17p loss, and 1q gain) in tumor initiation, together with persistent events contributing to the complex landscape of genomic ITH (Fig. 1H).

The clinical success of ivosidenib (2) and pemigatinib (3) may be attributed to the clonality of *IDH1* mutation and *FGFR2* fusion, respectively (Fig. 1A). Considering the prevalence of driver mutations in three other iCCA cohorts (19–21), we identified *KRAS*, *PIK3CA*, *ARID1A*, *ATM*, *BRCA1*, and *BRCA2* mutations as the most promising therapeutic targets (Fig. 1I). *KRAS* mutations occurred in 7.5% to 26.7% of patients with iCCA, presenting as hotspot mutations such as *KRAS*^{G12D} and *KRAS*^{G12V}. Recently, multiple small molecules, including AMG510, MRTX849, and JNJ-74699157, have been developed to target *KRAS*^{G12C} specifically (22–24). However, *KRAS*^{G12D}, instead of *KRAS*^{G12C}, was the dominant mutant in iCCA but still lacked specific inhibitors. Gain-of-function mutations in *PIK3CA* occurred in 3.2% to 8.9% of patients, and those patients were ideal candidates for alpelisib treatment (25). Loss-of-function alterations in *BRCA1*, *BRCA2*, *ATM*, and *ARID1A*, occurring in 15.0% to 37.8% of patients, damaged homologous recombination repair and conferred sensitivity to PARP inhibitors such as olaparib (26).

Heterogeneous Immune Infiltration and Extensive T-cell Exclusion

To explore the influence of genomic ITH on the immune microenvironment, we used the immune signature by DanaHER and colleagues (27) to characterize the immune context (Supplementary Fig. S4A and S4B; Supplementary Table S2). At the tumor region level, unsupervised hierarchical clustering stratified 205 tumor regions into two distinct clusters: high (85 regions from 33 patients) and low (120 regions from 38 patients) immune infiltration (Fig. 2A). Nearly all immune cell subgroups exhibited positive correlations, especially for lymphocyte subsets (Supplementary Fig. S4C). Strong positive correlations of transcriptomic immune deconvolution with multiplexed immunostaining results and histologic tumor-infiltrating lymphocyte (TIL) estimates were observed (Supplementary Fig. S4D and S4E). As expected, the high-infiltration cluster showed a significantly higher level of histologic TILs, intense immunostaining densities of CD3⁺ T cells, CD8⁺ T cells, and CD68⁺ macrophages ($P < 0.001$; Supplementary Fig. S4F and S4G), and elevated cytolytic activity (CYT; ref. 28) and IFN γ signature (29), indicating stronger immune responses in these regions ($P < 0.001$; Supplementary Fig. S4H). Intriguingly, the high-infiltration cluster displayed comparable tumor mutation burden (TMB)

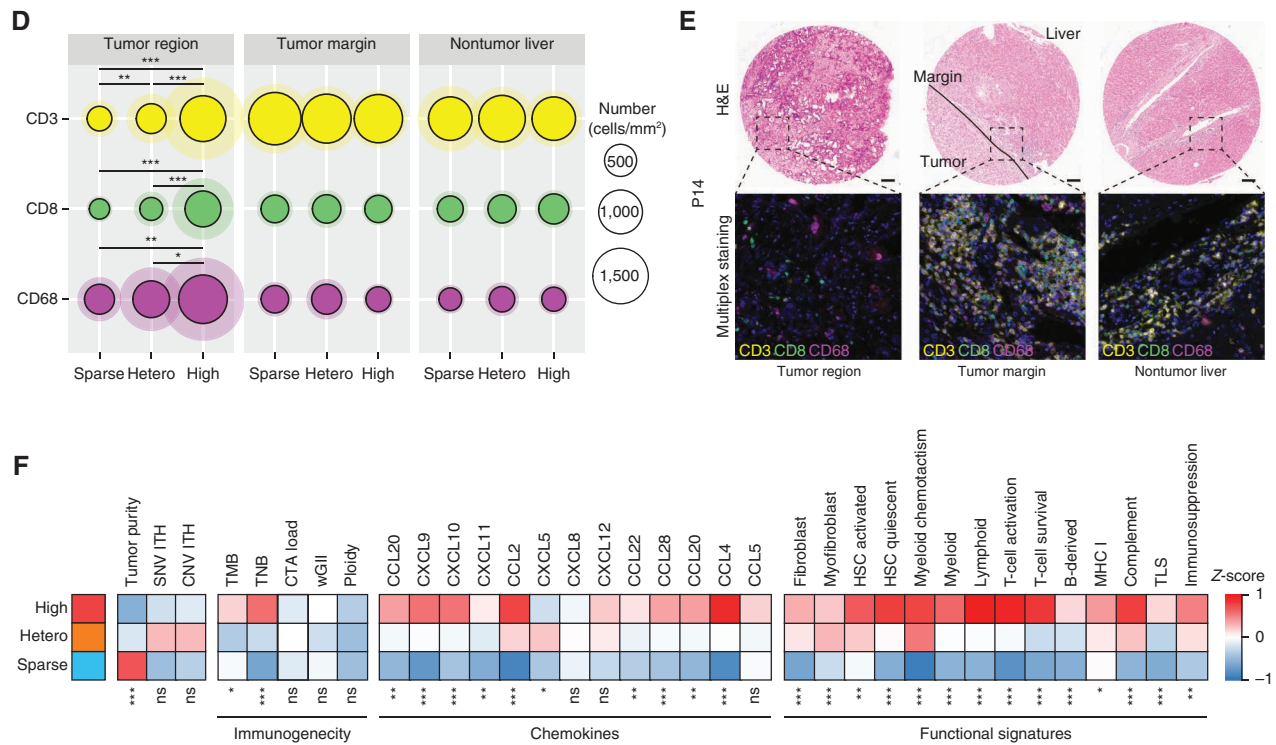


Figure 2. (Continued) **D**, Circle plots showing mean and standard deviation (SD) of cell densities in tumor regions, tumor margins, and nontumor livers per mm² for CD3 (yellow), CD8 (green), and CD68 (purple); Mann-Whitney test, **P* < 0.05; ***P* < 0.01; ****P* < 0.001; ns, not significant. **E**, Representative hematoxylin and eosin (H&E) and multiplex staining images showing the T-cell exclusion in P14 (a sparsely infiltrated tumor). Scale bars, 200 μm. **F**, Heat map showing immunogenomic characteristics among the three immune groups; Kruskal-Wallis test. CTA, cancer testis antigen; HSC, hepatic stellate cell; MHC, major histocompatibility complex; TLS, tertiary lymphoid structure; wGII, weighted genome instability index.

but significantly higher tumor neoantigen burden (TNB), implying that the immunogenicity of mutations might direct immune infiltration (Supplementary Fig. S4I).

At the patient level, the 45 patients were stratified into three immune groups: sparsely infiltrated (uniformly low immune infiltration across subregions, 12 patients containing 52 regions), heterogeneously infiltrated (heterogeneous immune infiltration among subregions, 26 patients containing 120 regions), and highly infiltrated (uniformly high immune infiltration across subregions, 7 patients containing 33 regions; Fig. 2A). Heterogeneous infiltration among different tumor regions was further confirmed by multiplex immunostaining and histology (Fig. 2B; Supplementary Fig. S4J). We applied four published transcriptome-based immunophenotypic classifiers (30–33) to stratify our multi-region samples, revealing that the heterogeneously infiltrated group harbored higher proportions of tumor subregions distributed in different immunophenotypes within the same patients (Fig. 2C; Supplementary Fig. S5A). Likewise, the IFN γ signature was also more variant in this group (Supplementary Fig. S5B). The results highlighted the challenges in the immune stratification and immunotherapy prediction of iCCA patients with a single biopsy.

As evaluated by multiplexed immunostaining on tumor microarrays (TMA; including matched tumor subregions, tumor margin, and nontumor liver; Supplementary Fig. S1B), the three immune groups displayed comparable densities of CD3⁺ T cells, CD8⁺ T cells, and CD68⁺ macrophages in

tumor margins and nontumor livers but significantly differed in tumor subregions (Fig. 2D). T-cell exclusion was sequentially aggravated from highly infiltrated to sparsely infiltrated tumors (Fig. 2E). In contrast, macrophages were more abundant in tumor regions than in surrounding tissues (Supplementary Fig. S5C), suggesting that T cells were the targets of exclusion. Immunogenomic analysis showed that highly infiltrated tumors displayed comparable cancer testis antigen (CTA) load, chromosomal instability, and ploidy with heterogeneously and sparsely infiltrated tumors but had significantly higher TNB and the lowest tumor purity (Fig. 2F). Sparsely infiltrated tumors had comparable TMB and TNB with heterogeneously infiltrated tumors but exhibited universally fewer immune and stromal cells. Meanwhile, multiple chemokines, including *CXCL9*, *CXCL10*, and *CXCL11*, were inadequate in sparsely infiltrated tumors compared with highly infiltrated tumors, and heterogeneously infiltrated tumors displayed the distinct distribution of chemokines between tumor subregions with low and high immune infiltration (Fig. 2F; Supplementary Fig. S5D). We then compared transcriptomic features among the three immune groups using hallmarks from the Molecular Signatures Database (MSigDB; ref. 34). Immune-related pathways, angiogenesis, and classical cancer pathways were upregulated in highly infiltrated tumors, while sparsely infiltrated tumors upregulated cell-cycle signaling and several metabolic pathways such as oxidative phosphorylation and cholesterol homeostasis (Supplementary Fig. S5E). These results revealed distinct

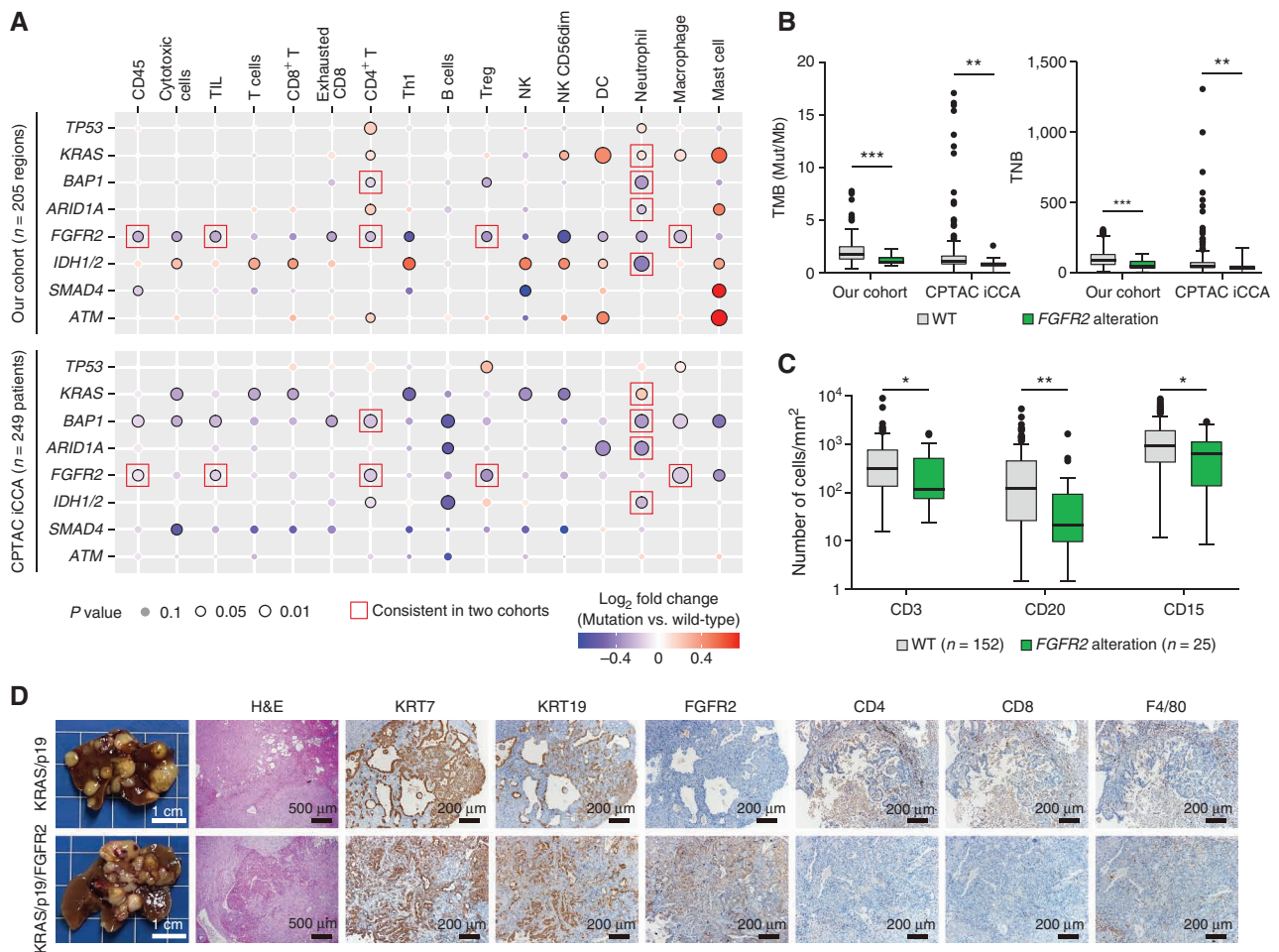


Figure 3. The impact of *FGFR2* alterations on the immune microenvironment. **A**, Correlations between recurrent gene alterations and immune infiltration in our cohort (top) and the CPTAC cohort (bottom); Mann-Whitney test. Consistent relationships are highlighted with the red frame. DC, dendritic cell; NK, natural killer; Treg, regulatory T cell. **B**, Box plots comparing TMB (left) and TNB (right) between iCCA samples with and without *FGFR2* alterations in our cohort and the CPTAC cohort; Mann-Whitney test. Mut/Mb, mutations per megabase; WT, wild-type. **C**, Box plots comparing CD3⁺ T cells, CD20⁺ B cells, and CD15⁺ neutrophils as measured by immunostaining between tumors with *FGFR2* alterations and WT in the CPTAC cohort; Mann-Whitney test, *, $P < 0.05$; **, $P < 0.01$; ***, $P < 0.001$. **D**, Representative photographs, hematoxylin & eosin (H&E) staining, and indicated immunostaining images of mouse KPF and KP tumors. (continued on following page)

immune landscape, genomic, and transcriptomic characteristics among the three immune groups. We further calculated an immune ITH index for each patient and observed significant positive correlations between ITH of genomic features and immune contexts, indicating their potential interaction (Supplementary Fig. S5F).

***FGFR2* Alteration Correlates with Less Immune Infiltration**

A specific genetic profile could affect the infiltration and composition of immune cells in the tumor microenvironment (35). We combined the multiomics data of our cohort and the CPTAC iCCA cohort to investigate the correlations between recurrent gene alterations and immune groups (Fig. 3A; Supplementary Table S3). The result showed that iCCA with *KRAS* mutations had a tendency for more myeloid infiltration but fewer lymphocytes (Fig. 3A), reflecting its role in reprogramming the local milieu to support tumor progression (36, 37). Contrarily, negative correlations were found between *BAP1* or *ARID1A* mutations and neutrophil infiltration (Fig. 3A).

Recent studies reported that *IDH1/2* mutations could shape a “cold” immune microenvironment in iCCA (14, 38), but patients with *IDH1/2* mutations displayed more T-cell infiltration in our cohort. We found that three of the eight cases with *IDH1/2* mutations were highly infiltrated tumors, with two of them having hepatitis B virus (HBV) infection and the rest showing a relatively high TNB (ranking 2/45 in our cohort). HBV infection positively correlated with lymphocyte infiltration in iCCA, similar to the finding in hepatocellular carcinoma (39), irrespective of *IDH1/2* mutation or wild-type (Supplementary Fig. S6A and S6B). Thus, the immune impact of *IDH1/2* mutations could be influenced by coexisting factors such as hepatitis and neoantigenicity, which may explain the unexpected genotype-immune correlations in our cohort. Indeed, in patients with HBV infection ($n = 69$) and liver cirrhosis ($n = 22$) from the CPTAC cohort, *IDH1/2* mutations also showed a trend of positive correlations with immune infiltration (Supplementary Fig. S6C).

FGFR2 fusion is a fascinating drug target in iCCA (6), but its influence on the immune microenvironment remains unclear.

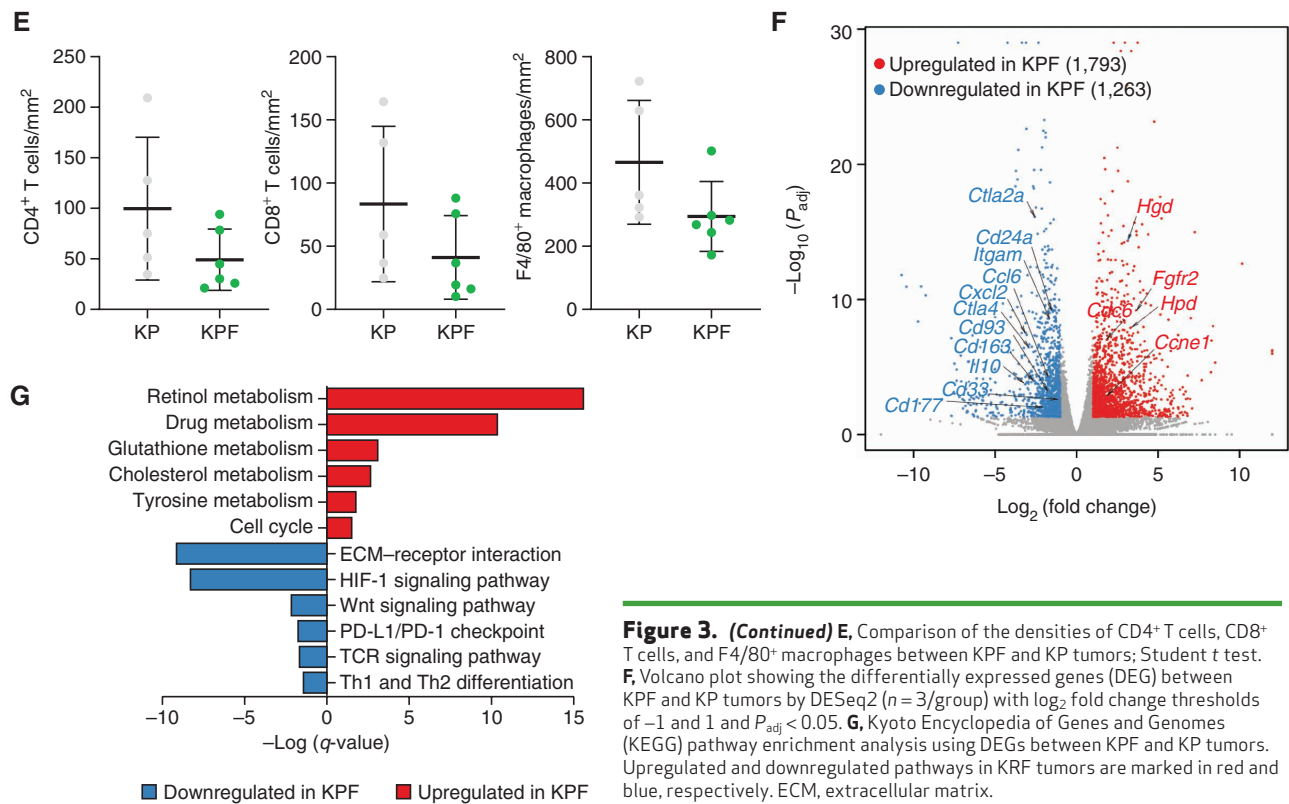


Figure 3. (Continued) E, Comparison of the densities of CD4⁺ T cells, CD8⁺ T cells, and F4/80⁺ macrophages between KPF and KP tumors; Student t test. F, Volcano plot showing the differentially expressed genes (DEG) between KPF and KP tumors by DESeq2 ($n = 3/\text{group}$) with \log_2 fold change thresholds of -1 and 1 and $P_{\text{adj}} < 0.05$. G, Kyoto Encyclopedia of Genes and Genomes (KEGG) pathway enrichment analysis using DEGs between KPF and KP tumors. Upregulated and downregulated pathways in KRF tumors are marked in red and blue, respectively. ECM, extracellular matrix.

Notably, *FGFR2* alterations (fusion and mutation) were consistently associated with fewer immune cells, including total TILs, CD4⁺ T cells, and macrophages, together with lower TMB and TNB, in both our cohort and the CPTAC cohort (Fig. 3A and B). Downregulation of immune-related pathways and genes of cytotoxicity, chemotaxis, immune exhaustion, and inhibition was noted in iCCA with *FGFR2* alterations (Supplementary Fig. S7A and S7B). Immunostaining on the TMA ($n = 177$) of the CPTAC cohort verified that iCCA with *FGFR2* alterations had fewer CD3⁺ T cells ($P = 0.033$), CD20⁺ B cells ($P = 0.003$), and CD15⁺ neutrophils ($P = 0.030$) than wild-type tumors (Fig. 3C; Supplementary Fig. S7C). Furthermore, we constructed murine iCCA models with or without an *FGFR2::BICC1* fusion by a hydrodynamic tail-vein injection. *KRAS/p19/FGFR2* (KPF) and *KRAS/p19* (KP) models led to macroscopic isolated iCCA tumors, whereas *AKT/YAP/FGFR2* (AYF) and *AKT/YAP* (AY) models resulted in diffuse iCCA nodules in the liver (Fig. 3D; Supplementary Fig. S7D). KPF and AYF tumors had fewer CD4⁺ T cells, CD8⁺ T cells, and F4/80⁺ macrophages than KP and AY tumors, respectively, highlighting the repressed immune microenvironment by the *FGFR2::BICC1* fusion protein (Fig. 3E; Supplementary Fig. S7E). RNA-seq analysis identified 3,055 differentially expressed genes between KPF and KP tumors, including downregulation of *Cxcl2*, *Ccl6*, *Cd163*, *Cd24a*, *Cd177*, and *Ctla4* in KPF tumors (Fig. 3F). Downregulated genes in KPF tumors were enriched in immune responses like Th1/Th2 differentiation, TCR signaling, and immune checkpoint pathways, whereas upregulated genes were involved in pathways of multiple metabolic processes (Fig. 3G), consistent with the above findings in human samples.

Distinct Neoantigen Depletion Mechanisms among Three Immune Groups

Neoantigen depletion is a common immune escape mechanism of tumors (40). Like mutations, neoantigens also showed significant ITH where only a median of 36.1% (range, 9%–60%) were identified as clonal (Supplementary Fig. S8A; Supplementary Table S4). Highly infiltrated tumors tended to have more clonal and subclonal neoantigens, but the ratios of clonal neoantigens were comparable among the three immune groups (Supplementary Fig. S8B and S8C). Considering the complex process from gene mutations to neoantigen presentation, we only analyzed clonal neoantigen depletion at DNA (through copy-number loss), mRNA (through expression silence), and presentation levels [through loss of heterozygosity (LOH) of HLA]. At least half of clonal neoantigens could not be presented, where copy-number loss, expression silence, and HLA LOH led to the depletion of 2.2%, 47.1%, and 3.8% of clonal neoantigens, respectively (Fig. 4A).

Copy-number loss of clonal neoantigens occurred in 17.6% (36/205) of tumor regions, leading to 2.3% (46/2,034), 2.9% (152/5,164), and 0.9% (29/3,239) of clonal neoantigen depletion in sparsely, heterogeneously, and highly infiltrated tumors, respectively (Supplementary Fig. S8D). We compared clonal neoantigens with nonneoantigenic, nonsynonymous clonal mutations to determine whether clonal neoantigen loss is an active event as previously described (40). Clonal neoantigen loss occurred more frequently than their nonneoantigenic counterparts in sparsely ($P = 0.002$) and heterogeneously infiltrated tumors ($P = 0.046$), indicating active clonal neoantigen loss in those tumors but not in highly infiltrated tumors ($P = 1.00$; Fig. 4B). Further

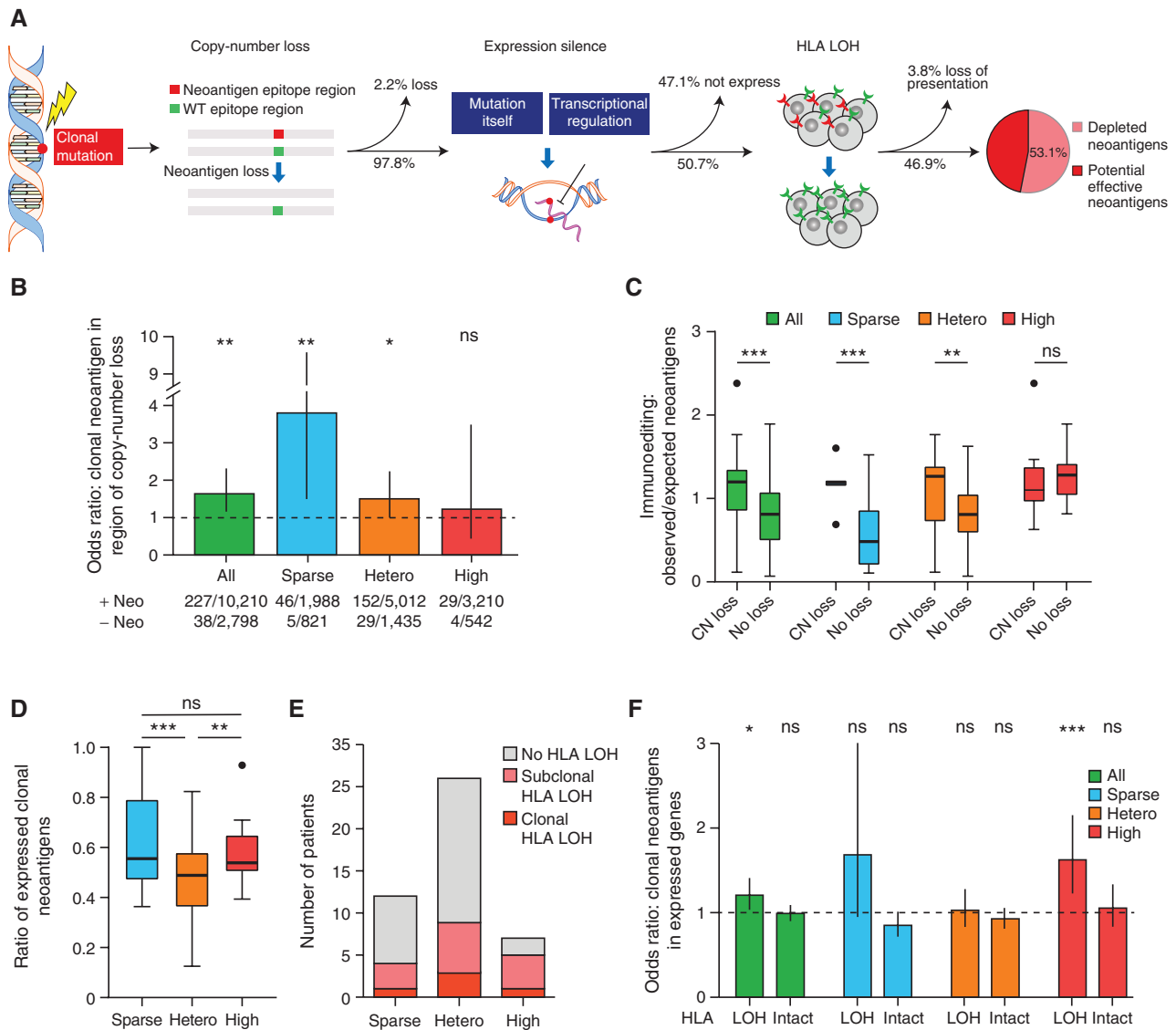


Figure 4. Neoantigen depletion in iCCA. **A**, A diagram illustrating clonal neoantigen depletion in iCCA. WT, wild-type. **B**, The odds ratio of clonal neoantigen depletion through copy-number loss compared with nonneoantigenic, nonsynonymous clonal mutations in the three immune groups; Fisher exact test, *, $P < 0.05$; **, $P < 0.01$; ***, $P < 0.001$; ns, not significant. Values >1 suggest that clonal neoantigens are more likely to exist in regions of copy-number loss than their nonneoantigenic counterparts. **C**, Box plots showing immunoeediting scores of tumor regions with clonal neoantigen (CN) loss and those without clonal neoantigen loss; Mann-Whitney test. **D**, Comparison of the proportions of expressed clonal neoantigens among the three immune groups; Mann-Whitney test. **E**, Events of clonal and subclonal HLA LOH in the three immune groups. **F**, The odds ratio of expressed clonal neoantigens compared with nonneoantigenic, nonsynonymous clonal mutations in the three immune groups divided by HLA LOH or not; Fisher exact test. Values >1 suggest that clonal neoantigens are more likely to be expressed than their nonneoantigenic counterparts. (continued on following page)

dissection of heterogeneously infiltrated tumors showed that tumor regions with low infiltration, instead of high infiltration, actively abandoned clonal neoantigens through copy-number loss, authenticating the above assumption (Supplementary Fig. S8E). We then quantified the DNA immunoeediting score in each tumor region, where the lower score indicates stronger DNA immunoeediting (28). Intriguingly, tumor regions with clonal neoantigen loss exhibited weaker DNA immunoeediting than those without clonal neoantigen loss in sparsely and heterogeneously infiltrated tumors (Fig. 4C), suggesting that DNA immunoeediting was a supplement to clonal neoantigen loss.

Mutated gene silence could be directed by mutation itself or transcriptional regulation. A median of only 52.0% (range, 12.5%–100%) of clonal neoantigens were expressed in iCCA, and the proportion was significantly lower in heterogeneously infiltrated tumors (median, 48.8%) than in sparsely infiltrated tumors (median, 55.6%; $P < 0.001$; Fig. 4D), partly reflecting the selection of neoantigen expression under immune pressure. However, this proportion rebounded to 53.8% in highly infiltrated tumors, possibly due to the extensive defects in antigen presentation machinery and T-cell exhaustion in this group (described below). Alternatively, other potential mechanisms, such as epigenetic silence by

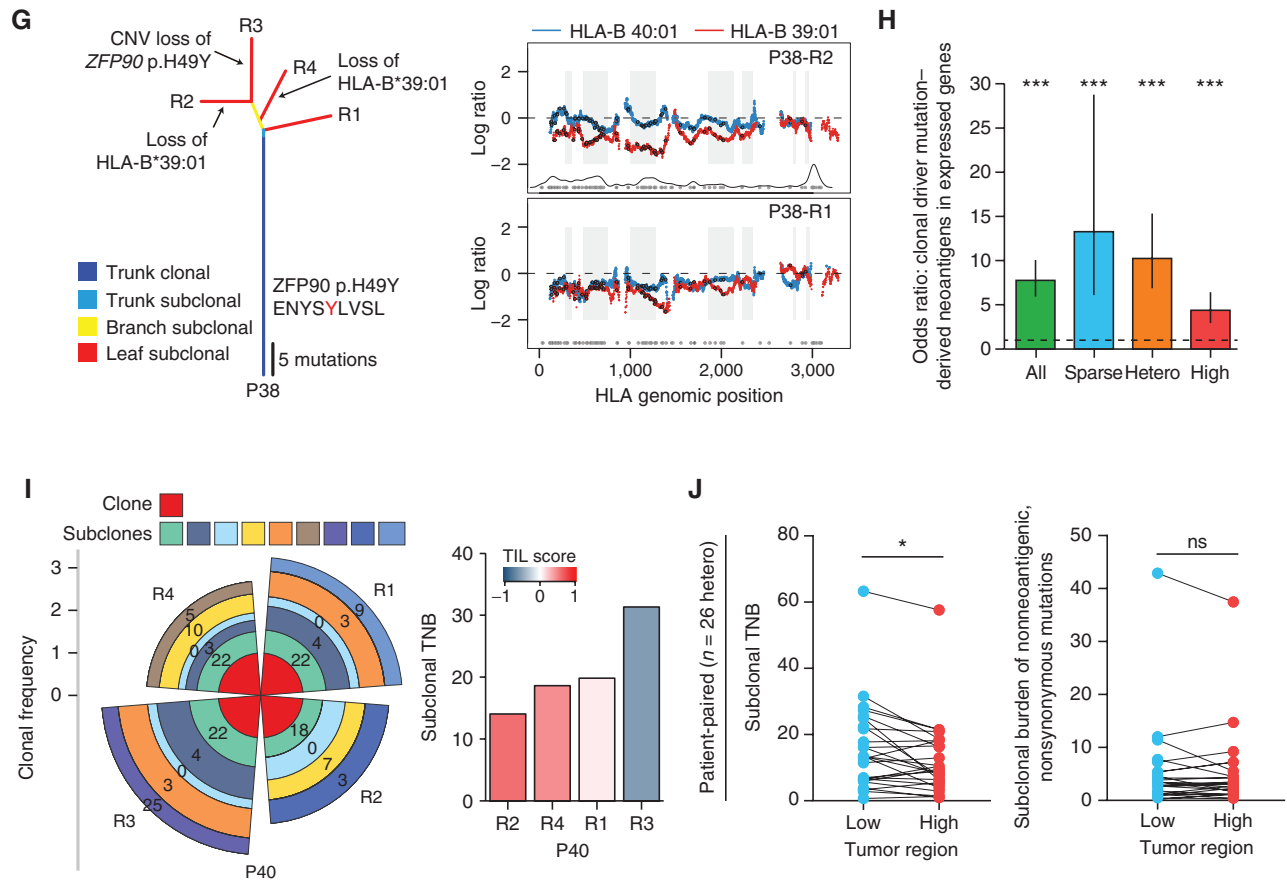


Figure 4. (Continued) **G**, Parallel clonal neoantigen depletion in P38. **H**, The odds ratio of expressed clonal driver mutation-derived neoantigens compared with clonal nondriver mutation-derived neoantigens in three immune groups; Fisher exact test. Values >1 suggest that clonal driver mutation-derived neoantigens are more likely to be expressed than clonal nondriver mutation-derived neoantigens. **I**, A typical example of heterogeneously infiltrated tumors in which subclonal TNB shows a negative correlation with TIL score. Coxcomb plot presenting the subclonal architecture (left) and histogram showing the subclonal TNB and TIL score (right) in different tumor regions of P40. The length of the coxcomb plot represents the clonal frequency of tumor subclones, and the neoantigen number of each subclone is noted. **J**, Comparisons of subclonal TNB (left) and subclonal mutation burden of nonneoantigenic, nonsynonymous mutations (right) between tumor regions with low and high infiltration within heterogeneously infiltrated tumors; paired Wilcoxon test.

DNA methylation (41), may also exist, which is beyond the scope of this study. We indeed observed a higher frequency of HLA LOH in highly infiltrated tumors (71.4%, 5/7) than heterogeneously (34.6%, 9/26) or sparsely infiltrated (33.3%, 4/12; Fig. 4E) tumors. For highly infiltrated tumors, clonal neoantigens tended to be expressed more frequently than their nonneoantigenic counterparts in tumor regions with HLA LOH ($P < 0.001$; Fig. 4F), suggesting that HLA LOH might liberate clonal neoantigen from expression silence. Meanwhile, increased copy-number loss of *B2M*, *TAP1/TAP2*, and *HSPA1A/HSPA1B* in highly infiltrated tumors further damaged antigen presentation to avoid expression silence of clonal neoantigens compared with heterogeneously infiltrated tumors (Supplementary Fig. S8F and S8G).

Parallel evolution is a common phenomenon as a result of positive selection in tumors (42). We observed parallel clonal neoantigen depletions through distinct mechanisms in 17 of 45 tumors, more so in highly infiltrated tumors (5/7, 71.4%) than in sparsely (3/12, 25.0%) and heterogeneously infiltrated (9/26, 34.6%; $P = 0.086$) tumors. For example, the copy-number loss of *ZFP90*^{C145T} occurred in P38-R3, whereas the subclonal

loss of HLA-B 39:01 damaged the presentation of the neopeptide ENYSYLVS L derived from *ZFP90*^{C145T} in P38-R2 and R4, resulting in the depletion of *ZFP90*^{C145T}-derived neoantigens in P38-R2, R3, and R4 (a highly infiltrated tumor; Fig. 4G).

We also compared the clonal neoantigen depletion derived from driver and nondriver mutations. Copy-number loss of clonal nondriver mutation-derived neoantigens (225/9,872, 2.3%) occurred more frequently than those from driver mutations (2/565, 0.4%; Supplementary Fig. S8H). As such, significantly higher proportions of clonal driver mutation-derived neoantigens (499/565, 88.3%) were expressed than nondriver mutation-derived neoantigens (4,874/9,872, 49.4%) in all three immune groups (Fig. 4H). In terms of immunogenicity, driver mutations were predicted to produce significantly fewer and also less immunogenic neoantigens than nondriver mutations, which may represent innate immune evasion (Supplementary Fig. S8I).

The assessment of subclonal neoantigen depletion may be complicated by sequencing depth and tumor purity. Alternatively, we calculated subclonal TNB for each tumor, defined as the sum of subclonal neoantigen numbers multiplied by

corresponding cancer cell fractions (Supplementary Fig. S8J). Overall, within each patient, tumor regions with higher TIL scores exhibited significantly lower subclonal TNB compared with other regions ($P = 0.009$, linear mixed model). Such negative correlation was mainly contributed by heterogeneously infiltrated tumors ($P = 0.007$; Fig. 4I), as it disappeared in highly ($P = 0.114$) and sparsely infiltrated tumors ($P = 0.555$). To dissect the role of tumor purity, we calculated the subclonal burden of nonneoantigenic, nonsynonymous mutations using the same method. Indeed, subclonal TNB, rather than subclonal nonneoantigenic mutation burden, was significantly lower in regions with high versus low infiltration within heterogeneously infiltrated tumors (Fig. 4J). These findings highlighted the influence of heterogeneous immune infiltration on iCCA subclonal evolution.

Suppressive Microenvironment and T-cell Exhaustion Damage the Antitumor Effect

To further evaluate T-cell quality, we performed TCR-seq on all tumor samples and peripheral blood (one patient using nontumor liver tissue) and obtained an average of 18,776 (range, 52–115,446) unique TCR β rearrangements per tumor region. Compared with sparsely and heterogeneously infiltrated tumors, highly infiltrated tumors displayed more unique TCR clones but comparable TCR clonality (Supplementary Fig. S9A and S9B). The peripheral blood of patients with highly and heterogeneously infiltrated tumors displayed more unique TCR clones but also comparable TCR clonality compared with the peripheral blood of patients with sparsely infiltrated tumors (Supplementary Fig. S9A and S9B). Then, we investigated the overlap of TCR clones across different tumor regions. Consistent with previous studies (43, 44), most TCR clones were unique to individual tumor regions, ranging from 38.7% to 79.9%, whereas there were also TCR clones ubiquitous among all regions of the tumor, with as little as 0.9% and at most 30.6% (Fig. 5A). The percentages of shared TCR clones across tumor regions and between tumor and peripheral blood were both significantly higher in highly infiltrated tumors, indicating that extensive intratumoral immune responses could also cause perturbations in the peripheral TCR repertoire (Supplementary Fig. S9C). The Morisita–Horn index (44) was calculated to measure the similarity of the TCR repertoires between two tumor regions within a tumor, and highly infiltrated tumors exhibited more similar TCR profiles across regions as expected (Supplementary Fig. S9D).

Of particular interest was P25 (a highly infiltrated tumor), who exhibited clonal copy-number loss of *B2M* and HLA-B 58:01, along with wide parallel subclonal mutations in the remaining *B2M* allele, including *B2M* p.L13 frameshift deletions in R1, R3, and R5, and a *B2M* 72–78 nonframeshift deletion in R2 (Supplementary Fig. S9E). Within P25, R4 exhibited the strongest subclonal immunoeediting with the lowest immune infiltration and TCR clonality, whereas the other four regions developed *B2M* mutations to further destroy antigen presentation (Supplementary Fig. S9E). Interestingly, TRBV4-1-TRBJ1-4 (CDR3aa: CASSQGQGREKLFF) and TRBV15-TRBJ1-2 (CDR3aa: CATSSGLSGADYGTYF) were dominant in P25-R1, R3, and R5, whereas P25-R2 exhibited a distinct TCR repertoire, which might be the result of different *B2M* mutation patterns and a subclonal neoantigen

profile, implying the interaction between tumor evolution and TCR composition.

Multiple immune checkpoints, including *PD-1*, *PD-L1*, and *CTLA4*, were serially overexpressed from sparsely infiltrated tumors to highly infiltrated tumors (Supplementary Fig. S9F). Sparsely infiltrated tumors exhibited comparable proportions of PD-1⁺CD8⁺ T cells with corresponding tumor margins and nontumor livers, whereas highly and heterogeneously infiltrated tumors showed significantly increased proportions over paired tumor margins and nontumor livers, indicating that CD8⁺ T cells were gradually programmed into an exhaustion phenotype (Fig. 5B; Supplementary Fig. S9G). Also, a higher proportion of PD-L1⁺ stromal cells was observed in highly infiltrated tumors (Fig. 5B; Supplementary Fig. S9H), and CD8⁺ T-cell exhaustion scores sequentially increased from sparsely to heterogeneously to highly infiltrated tumors (Supplementary Fig. S9I). In addition, highly and heterogeneously infiltrated tumors displayed more CD4⁺FOXP3⁺ regulatory T-cell (Treg) and CD206⁺ M2-like macrophage infiltration than sparsely infiltrated tumors (Fig. 5C; Supplementary Fig. S9J and S9K). All three groups exhibited a significantly higher proportion of Tregs and a lower ratio of CD8⁺ T cells/Tregs in tumor regions than in corresponding tumor margins and nontumor livers, highlighting the widespread immunosuppressive role of Treg accumulation in iCCA (Fig. 5C; Supplementary Fig. S9L).

We then integrated immune infiltration status and immune evasion mechanisms to predict patient prognosis, considering that immune diversity (i.e., sparse, hetero, and high immune groups) itself had minimal prognostic significance. Patients were classified as the low evasion group (highly or heterogeneously infiltrated with no evidence of HLA LOH or extreme CD8⁺ T-cell exhaustion) and the high evasion group (sparsely infiltrated or exhibiting evidence of HLA LOH or extreme CD8⁺ T-cell exhaustion; Fig. 5D). In our cohort, the high evasion group had significantly shorter recurrence-free survival than the low evasion group (HR = 2.24, $P = 0.040$; Fig. 5E). We also divided the CPTAC iCCA cohort into low and high evasion groups, and patients with high evasion ability had shorter overall survival (HR = 1.90, $P = 0.011$; Fig. 5F). Notably, immune evasion ability remained as an independent prognosticator in multivariable analysis in both cohorts (Supplementary Table S5). Again, a similar result was found in The Cancer Genome Atlas (TCGA) iCCA cohort ($n = 32$, HR = 3.62, $P = 0.046$), corroborating the robustness of the prognostic classification system (Fig. 5G).

Intrahepatic Metastases Share Similar Immune Features with the Original Clones

Intrahepatic metastasis (IM) is a common metastatic route of iCCA. We plotted phylogenetic trees and CNV profiles of four tumors with IMs and inferred the most likely tumor region origin for each metastasis (Fig. 6A and B). For example, P11-IM2 and P11-R2 had the closest clonal evolutionary trajectories and CNV profiles, indicating that P11-IM2 was disseminated from tumor clones in P11-R2 (Fig. 6A). There was no special enrichment of driver mutations or CNVs in metastases, and metastases could derive from tumor clones of different regions, suggesting that the whole tumor, rather than special clones, had the potential to disseminate.

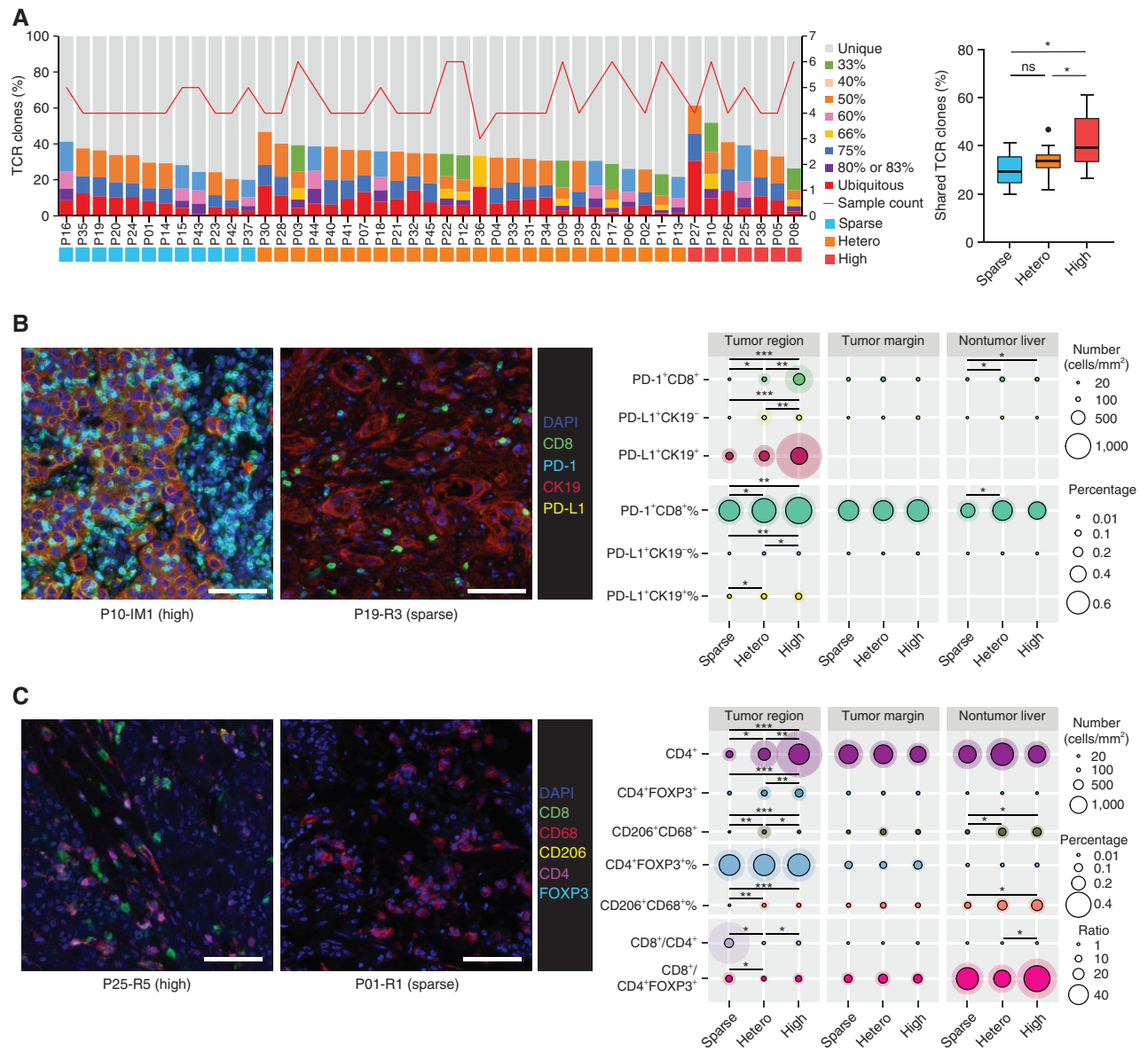


Figure 5. TCR landscape and suppressive microenvironment. **A**, Proportions of the top 0.02% of TCR clones detected in all regions, partial regions, and a single region of tumors (left) and box plots comparing the percentage of shared TCR clones among the three immune groups (right); Student *t* test, *, *P* < 0.05; **, *P* < 0.01; ***, *P* < 0.001; ns, not significant. The number of sampling tumor regions is indicated by the red line. **B**, Representative immunostaining images (left) of immune checkpoints in a highly and sparsely infiltrated tumor: CD8 (green), PD-1 (cyan), CK19 (red), PD-L1 (yellow), and DAPI (blue). Scale bars, 100 μm. Circle plots (right) showing mean and standard deviation (SD) of densities and proportions of indicated cells in tumor regions, tumor margin, and nontumor livers of the three immune groups; Mann-Whitney test. **C**, Representative immunostaining images (left) of Tregs and macrophages in a highly and sparsely infiltrated tumor: CD8 (green), CD68 (red), CD206 (yellow), CD4 (purple), FOXP3 (cyan), and DAPI (blue). Scale bars, 100 μm. Circle plots (right) showing mean and SD of densities and proportions as indicated in tumor regions, tumor margin, and nontumor livers of the three immune groups; Mann-Whitney test. (continued on next page)

Then, we performed unsupervised clustering based on the top 3,000 variant genes in each of the four patients (Supplementary Fig. S10A). There was no obvious separation between primary tumors and IMs, and the metastases even clustered together with the original tumor regions in 75.0% (6/8) of pairs. Unsupervised clustering using immune signatures of Danaher and colleagues (27) for each patient (Fig. 6C) showed that the IMs also clustered with original tumor regions in 75.0% (6/8) of pairs. Further immunostaining revealed that IMs exhibited similar infiltration of T cells and macrophages with their original tumor regions in P13

and P22 (Fig. 6D; Supplementary Fig. S10B). Overall, the metastatic clones with similar genomic and transcriptomic characteristics to primary clones within the same organ can shape a homologous immune microenvironment. Otherwise, distant metastases out of the original organ may generate distinct transcriptomic and immune profiles, despite stable genomic traits (45). Likewise, the TCR repertoire and high-frequency TCR clones were similar between paired primary tumors and IMs (Supplementary Fig. S10C and S10D), possibly due to the fact that they shared genomic features and consequently neoantigen profiles.

Downloaded from http://aacrjournals.org/aacrjournals/article-pdf/12/10/2350/321186/2350.pdf by guest on 29 September 2023

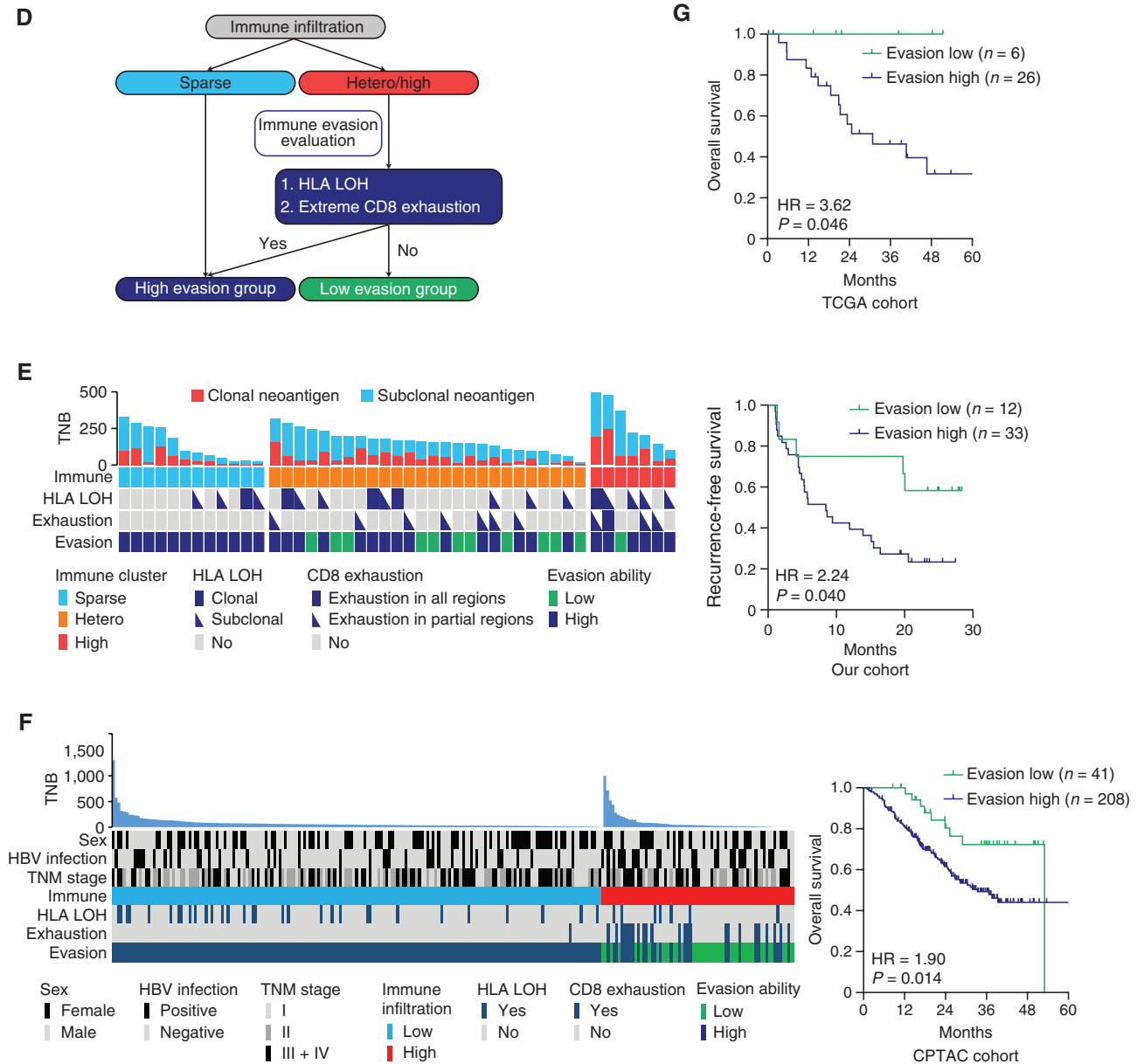


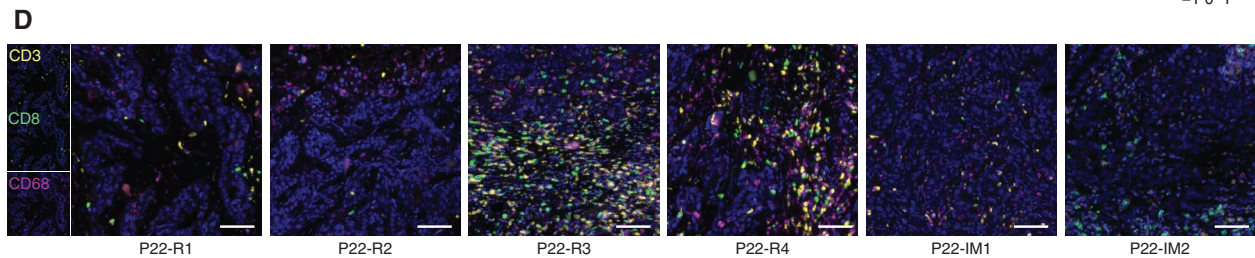
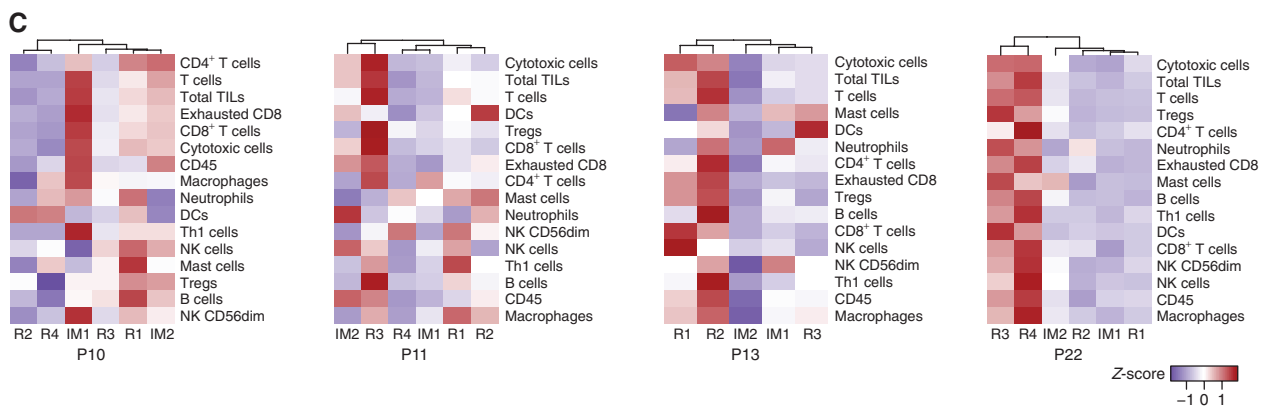
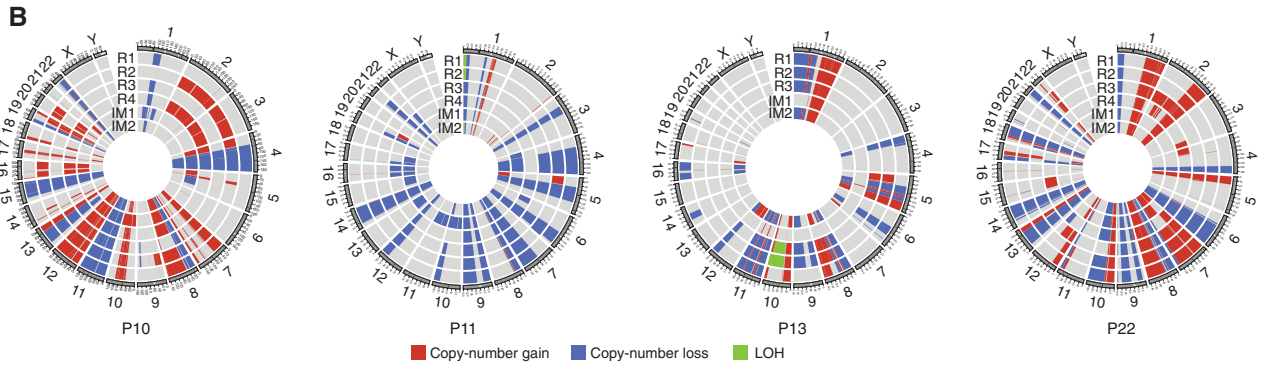
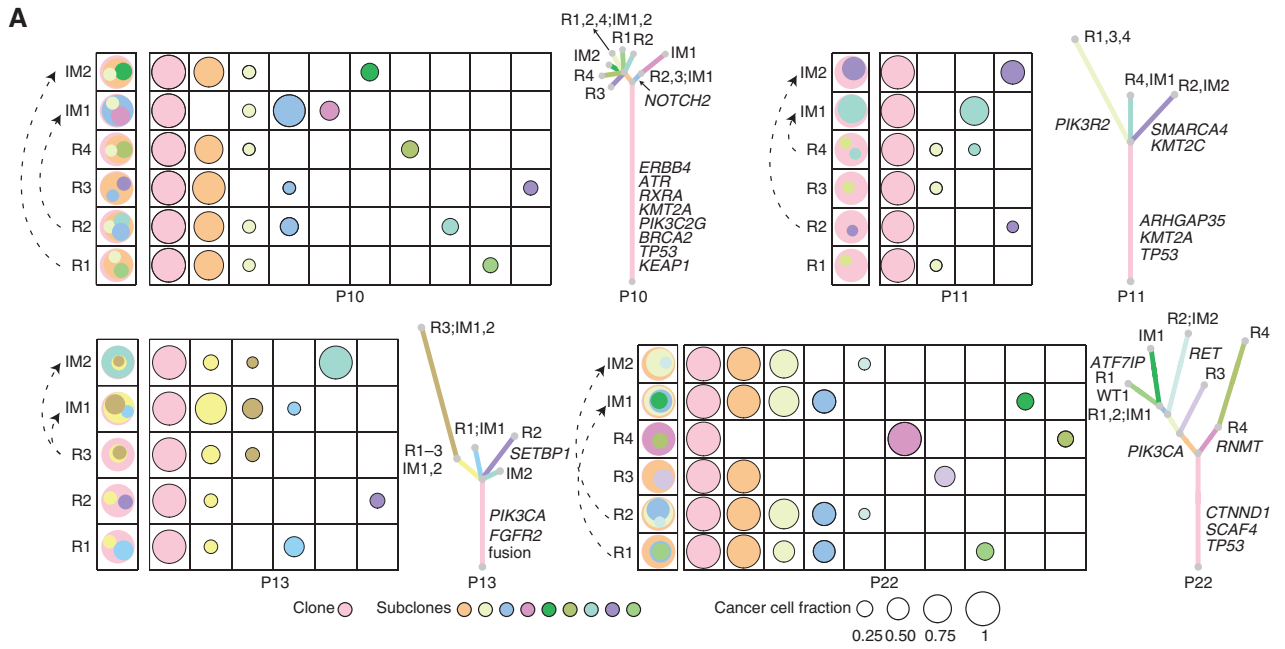
Figure 5. (Continued) **D**, A diagram for classifying patients into high and low immune evasion groups. **E** and **F**, Classification of patients into high and low immune evasion groups and corresponding Kaplan-Meier curves in our cohort (**E**) and the CPTAC cohort (**F**); log-rank test. TNM, tumor-node-metastasis. **G**, Kaplan-Meier curves for overall survival according to high and low immune evasion in the TCGA iCCA cohort; log-rank test.

LVVVGADGV (*KRAS*^{G12D}) Is a Potential Target for Personalized Immunotherapy

Neoantigens derived from driver mutations, such as *TP53*^{R175H} and *KRAS*^{G12D}, could activate a T-cell response, and neoantigen-specific T-cell clones could be used for adoptive cell therapy (46–48). Here, a total of 32 predicted neopeptides

from driver mutations of *TP53*, *KRAS*, *IDH1*, *IDH2*, and *BAP1* were synthesized to systematically estimate their potential as immunotherapeutic targets (Fig. 7A; Supplementary Fig. S1C; Supplementary Table S6). We used tetramer exchange experiments to evaluate the affinity of mutant peptides with HLA-A 02:01, HLA-A 24:02, and HLA-A 11:01

Figure 6. Clonal evolution and immune microenvironment of IMs. **A**, Clonal structure and phylogenetic trees of four tumors with IMs. Subclones with mutation numbers greater than or equal to 5 are shown, and the area of the circles is proportional to the cancer cell fraction of the corresponding subclone (left). The branch lengths are proportional to the number of mutations in each cluster in phylogenetic trees (right). The dotted lines indicate the inferred trajectories of intrahepatic dissemination. **B**, Circos plots showing CNV profiles of the primary and metastatic tumors. **C**, Hierarchical clustering of immune cell subgroups for four tumors. DC, dendritic cell; NK, natural killer. **D**, Representative immunostaining images of different regions in P22 for CD3 (yellow), CD68 (purple), CD8 (green), and DAPI (blue). Scale bars, 100 μ m.



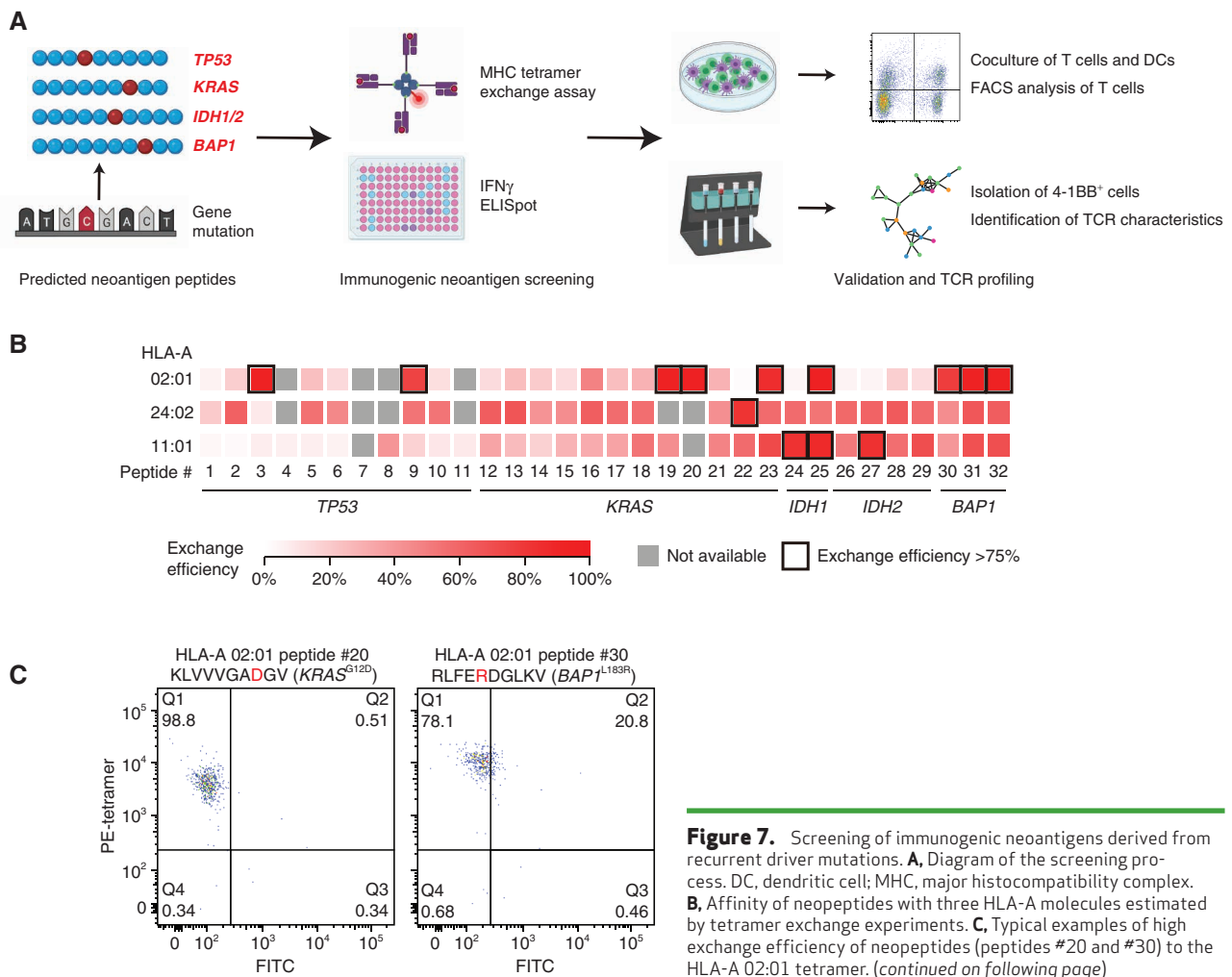


Figure 7. Screening of immunogenic neoantigens derived from recurrent driver mutations. **A**, Diagram of the screening process. DC, dendritic cell; MHC, major histocompatibility complex. **B**, Affinity of neopeptides with three HLA-A molecules estimated by tetramer exchange experiments. **C**, Typical examples of high exchange efficiency of neopeptides (peptides #20 and #30) to the HLA-A 02:01 tetramer. (continued on following page)

(the three most common HLA-A subtypes). The binding of peptides to HLA-A molecules was specific, where the same peptide could have completely different affinities with different HLA-A molecules (Fig. 7B; Supplementary Fig. S11A). The exchange efficiency was as high as 97.2% between peptide #3 and HLA-A 02:01, but as low as 7.8% between peptide #3 and HLA-A 11:01 (Fig. 7B), with 15.7% (13/83) of peptide-major histocompatibility complex (MHC) pairs defined as high affinity (exchange efficiency >75%; Fig. 7C).

In addition to the affinity with HLA molecules, the immunogenicity of peptides also determines their ability to stimulate immune cells. We isolated peripheral blood mononuclear cells (PBMC) from three healthy donors and performed an enzyme-linked immunosorbent assay (ELISpot) to quantify IFN γ secretion against different peptides (Fig. 7D). Strong reactivity against peptide #19 (LVVVGADGV, KRAS^{G12D}), peptide #29 (SQEQPRCHY, IDH2^{R37C}), and peptide #30 (RLFERDGLKV, BAP1^{L183R}) was detected in donor #1, whereas donors #2 and #3 showed only moderate reactivity against peptide #19 (Fig. 7D). Because dendritic cells are powerful antigen-presenting cells to prime T-cell responses (49), we further isolated peripheral monocytes from donor #4 and loaded them with antigen peptides (peptides #19, 20, 29, and 30 and the combined peptide pool) during

the differentiation into dendritic cells. Paired T cells were then cocultured with mature dendritic cells. Subsequent flow cytometry analysis of T-cell activation markers 4-1BB and CD107a demonstrated the enhanced reactivity of both CD4⁺ and CD8⁺ T cells against peptide #19 (LVVVGADGV, KRAS^{G12D}), which was superior to other peptides and comparable with the combined peptide pool (Fig. 7E; Supplementary Fig. S11B).

To identify peptide #19-specific TCR repertoire, we isolated activated 4-1BB⁺ cells stimulated by peptide #19 or DMSO (control) from donors #1 to 3 and performed TCR sequencing. TRBV9-TRBJ2-1 and TRBV25-1-TRBJ2-1 rearrangements were significantly enriched in the top 100 CDR3s whose frequencies varied mostly between peptide #19 and DMSO groups (Fig. 7F). We then used the GLIPH algorithm (50) to cluster potential peptide #19-specific activated CDR3 library (Supplementary Fig. S11C), and most of the TCR β sequences fell in one or few related TCR repertoires, among which the motifs RAGQ and KVD were identified (Fig. 7G). This preliminary screening indicated that LVVVGADGV (KRAS^{G12D}) had strong immunogenicity that can induce specific V-J rearrangements and TCR β motifs, which could be further exploited for personalized immunotherapy.

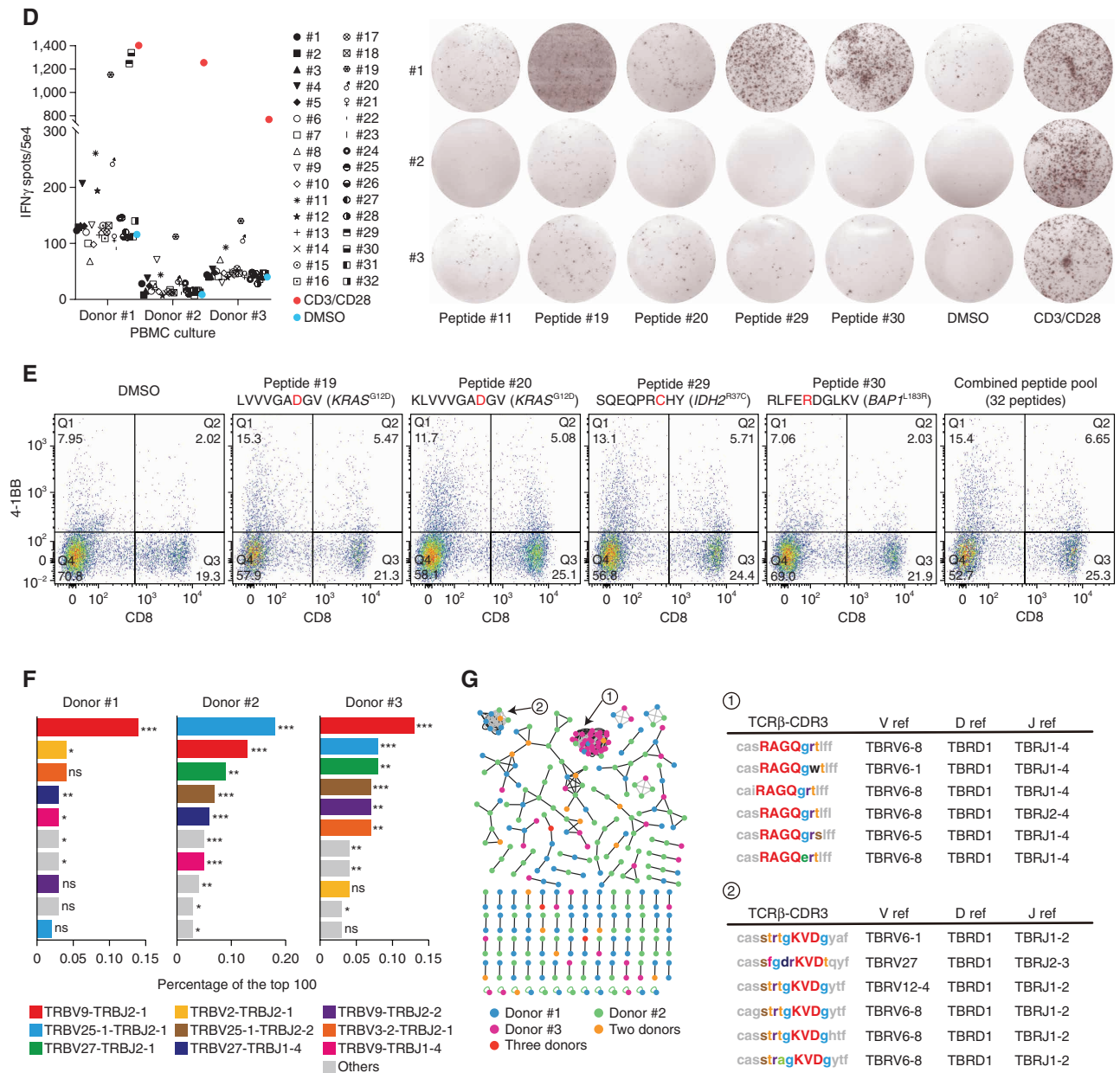


Figure 7. (Continued) D, IFN γ ELISpot assay results of three donors' PBMCs after coculture with neopeptides after 20 hours (left). DMSO (peptide vehicle) and CD3/CD28 T-cell activator were used as negative and positive controls, respectively. Representative images are shown on the right. **E**, Flow cytometry for 4-1BB on T cells after coculture with dendritic cells presenting different neoantigen peptides. **F**, V-J rearrangements of three donors in the top 100 CDR3s whose frequencies varied mostly between peptide #19 and DMSO groups. Fisher exact test, *, $P < 0.05$; **, $P < 0.01$; ***, $P < 0.001$; ns, not significant. **G**, GLIPH clustering of peptide #19-specific activated CDR3 library (left). Black arrows indicate representative clustering groups, accompanied by representative TCR β motifs (right).

DISCUSSION

Through the integration of genomic, transcriptomic, and immunophenotypic data, our study elucidates the dynamic interactions between iCCA evolution and the immune micro-environment. We observed intratumoral heterogeneous immune infiltration in more than half of iCCA, posing a great challenge for the immune classification of patients and the prediction of immunotherapeutic efficacy by single biopsy. Tumors were classified into three immune groups with distinct immune microenvironment characteristics and

neoantigen depletion mechanisms (Supplementary Fig. S11D), providing a novel insight to guide future immuno-oncologic therapeutic strategies.

Despite extensive genomic ITH in iCCA, some recurrent gene alterations, such as *TP53*, *KRAS*, *FGFR2*, *BAP1*, *PIK3CA*, *ATM*, and *IDH1/2*, were primarily clonal, providing considerable reliability to assess these mutations from a single biopsy and highlighting their potential as therapeutic targets. Among them, we found that *FGFR2*-altered iCCA displayed higher *FGFR2* expression and less immune infiltration, together with low TMB and TNB. Recently, Palakurthi and

colleagues (51) combined an FGFR inhibitor (erdafitinib) and anti-PD-1 therapy to treat an *FGFR2*-mutated lung cancer mouse model and induced significant tumor regression, with increased cytotoxic T-cell infiltration and decreased Tregs, macrophages, and PD-L1 expression. The finding raises the possibility that *FGFR2* inhibitors may drive the immunologic alterations and sensitize *FGFR2*-altered iCCA to anti-PD-1 therapy. Surprisingly, we revealed that *IDH1/2* mutations may not uniformly lead to sparse immune infiltration, but rather may be reversed by hepatitis virus infection and comutation profiles. This is analogous to Epstein-Barr virus-associated iCCA, which had abundant lymphocyte infiltration and was sensitive to ICIs compared with non-virus-associated iCCA (52).

A tumor must have developed immune evasion mechanisms to survive and grow *in vivo*. Neoantigen depletion could reduce the immunogenicity of tumor cells and serve as a major escape mechanism, which was observed during tumor recurrence (53), metastasis (54), and immunotherapy (55). Consistent with the finding in lung cancer (40), active clonal neoantigen loss mainly occurred in low-infiltration tumor regions in iCCA. We further found that DNA immunoeediting, which reflects the reprogramming of somatic mutations to produce fewer neoantigens (28), was complementary to clonal neoantigen loss in low-infiltration tumor regions. Both of them may represent tumor-intrinsic ways at the genomic level to immune escape. Previous studies in colorectal cancer and hepatocellular carcinoma have shown that DNA immunoeediting was prevalent in tumors with abundant T-cell infiltration but always lacking in those with HLA LOH (44, 54). These phenomena collectively suggest that different immune escape mechanisms may be dominant in distinct contexts, and pervasive antigen presentation disruption may explain the relatively low level of DNA immunoeediting in highly infiltrated iCCA in our study.

At the mRNA level, expression silence of clonal neoantigens was prevalent, especially in heterogeneously infiltrated tumors. Of note, highly infiltrated tumors displayed a comparable expression ratio of clonal neoantigens with sparsely infiltrated tumors. One hypothesis is that frequent antigen presentation defects may relieve the expression silence, because highly infiltrated tumors with HLA LOH exhibited a significant increase of expressed clonal neoantigens compared with their nonneoantigenic counterparts. We assume that highly infiltrated iCCA resemble microsatellite instability-high (MSI-high) colorectal cancers in the following aspects: (i) abundant immune infiltration, (ii) high neoantigen burden, (iii) frequent disruption to antigen presentation, and (iv) overexpression of immune checkpoints (56, 57). These similarities suggest that highly infiltrated iCCA could be suitable candidates for immune-checkpoint blockade. Considering that DNA hypermethylation is one of the important causes of neoantigen expression silence in iCCA (17, 58), heterogeneously infiltrated tumors may be optimal for the combination of epigenetic regulators and anti-PD-1 (Supplementary Fig. S11D). These conclusions are based on an in-depth analysis of the multiomics data, and further functional validation would solidify the findings.

Extrinsic immune escape mechanisms also played a critical role in tumor immune tolerance (59). T-cell exclusion was

extensive in iCCA, engendering the formation of immune-privileged microenvironments, especially in sparsely infiltrated tumors. Imbalanced CD8⁺ T cell/Treg was an essential characteristic of iCCA regardless of the abundance of immune infiltration as previously reported (60). Unsurprisingly, high immune infiltration was also accompanied by immune-checkpoint overexpression and CD8⁺ T-cell exhaustion, explaining why tumors can still exist in “hot” microenvironments (61, 62). Meanwhile, abundant PD-L1⁺ myeloid cells and stromal cells such as cancer-associated fibroblasts increased in highly infiltrated tumors, which may further weaken antitumor-immune response (63–65). These immunosuppressive cells help promote the cultivation of a high-infiltrated but useless or even tumor-promoting microenvironment. As a result, immune infiltration alone may not be sufficient to distinguish the outcomes of patients with iCCA, and thus we developed a simple but robust prognostic classification system based on immune evasion ability.

Although driver mutations produced fewer and less immunogenic neoantigens, they underwent weak immunoeediting compared with passenger mutations, which indicates that driver mutation expression is required for tumor cell fitness but also exposes vulnerability to targeted or immune therapy. Therefore, driver mutation-derived neoantigens were better targets than passenger mutation-derived neoantigens because the latter can be easily edited through neoantigen depletion. In this regard, we screened a panel of recurrent mutation-derived neoantigens and demonstrated strong immunogenicity and high affinity to HLA-A 02:01 of LVVVGADGV (*KRAS*^{G12D}). Recently, Kadam and colleagues (66, 67) combined anti-PD-1 and vaccination of LVVVGADGV peptide to treat a *KRAS*^{G12D} lung cancer mouse model and induced 80% tumor eradication, further supporting it as an ideal target for personalized immunotherapy (68). Specific V-J rearrangements and TCRβ motifs were also identified by us, which may help design engineered TCR T cells (69) for patients with *KRAS*^{G12D} in the future.

In conclusion, our study comprehensively illustrated tumor-immune interactions by integrating multiomics in iCCA, demonstrating the spatiotemporally heterogeneous immunogenomic features across patients and within tumors. Future studies of paired pre- and posttreatment samples using high-resolution spatial omics and single-cell profiling may provide a greater understanding of these processes. Based on current and ongoing knowledge, new combinational immunotherapies may ultimately renovate the treatment paradigm and improve clinical outcomes of this fatal malignancy.

METHODS

Patients and Samples

We prospectively collected 207 tumor samples from 45 patients with iCCA who underwent curative resection from January 2019 to December 2019 at the Zhongshan Hospital of Fudan University. A cut fully bisecting the resected tumor was made, and representative spatially separated regions were collected at least 5 mm away from each other and tumor margin. Tumor margins (defined as the region within 500 μm on each side of the border; ref. 70) and nontumor liver tissues (>2 cm away from tumor margin) were sampled from formalin-fixed, paraffin-embedded tissues to construct a TMA. This

study was approved by the Research Ethics Committee of Zhongshan Hospital (B2017-060R) with written informed consent from each patient and was conducted in accordance with ethical guidelines (Declaration of Helsinki).

WES, Variant Calling, and RNA-seq

WES and RNA-seq were performed by the DNBSEQ Platform (MGI Tech Co., Ltd.). Somatic mutations of tumor samples were detected using the blood samples or nontumor liver tissues as controls, and raw RNA data were processed as previously described (44). Detailed tissue preparation, data processing, and somatic mutation detection are described in Supplementary Materials and Methods.

Immune Infiltration Estimation

A total of nine published *in silico* immune tools (27, 28, 71–77) were collected and tested in our data (Supplementary Fig. S4A and S4B; Supplementary Table S2) as previously described (40). The proportion of genes in each method that met the criteria was calculated and further compared with multiplex immunofluorescence. Due to the lack of a CD4⁺ T-cell estimate in Danaher and colleagues (27), we used the estimate of CD4⁺ T cells from Shen and colleagues (75). Pathologic TILs were estimated using internationally established guidelines (www.tilsincancer.org; ref. 78).

Multiplexed Immunofluorescence

Multiplexed immunofluorescence was performed as we previously described (79). A total of four staining regimens were performed, and detailed information on antibodies is listed in Supplementary Table S2. Multispectral images of TMAs were scanned using Vectra 3.0 (PerkinElmer), and spectral unmixing was conducted using the inForm Advanced Image Analysis Software (v2.3 PerkinElmer) with built spectral libraries. Cutoff value for positivity was determined according to the staining patterns and intensities, and cell frequency was counted using R script.

Mouse Model Construction

Six-week-old, female FVB/N mice were ordered from the Shanghai Branch of Beijing Vital River Laboratory Animal Technologies Co. Ltd. The experiments were performed following the institutional guidelines strictly and were approved by the Institutional Animal Care and Use Committee (IACUC) of the Shanghai Branch of Beijing Vital River Laboratory Animal Technologies Co. Ltd. (2017-0014). pT3-EF1 α -HA-myr-Akt (mouse, Addgene, 31789, RRID: Addgene_31789) and pT3-EF1 α -YAP^{S127A} (human, Addgene, 86497, RRID: Addgene_86497) were obtained from Addgene (<https://www.addgene.org/>). The *FGFR2::BICC1* fusion gene and *KRAS*^{G12D} gene were synthesized and cloned into the pT3 vector, and the CRISPR/Cas9 single-guide RNA (sgRNA)-p19 was designed, synthesized, and cloned to the pX330 vector (Shanghai Xitubio Biotechnology Co., Ltd.). For the construction of AKT/YAP, AKT/YAP/FGFR2, KRAS/p19, and KRAS/p19/FGFR2 murine iCCA models, plasmids were injected into mice by the hydrodynamic tail-vein injection at a 10:1 ratio of transposon to SB-luc transposase-encoding plasmid (20 μ g of pT3-EF1 α -HA-myr-Akt plasmid, 30 μ g of pT3-EF1 α -YAP^{S127A} plasmid, 10 μ g of pT3-EF1 α -HA-FGFR2 fusion plasmid, 25 μ g of pT3-EF1 α -KRAS^{G12D} plasmid) as well as 10 μ g of the pX330-CRISPR/Cas9 sgRNA-p19 plasmid with the solution into the tail vein with a total volume corresponding to 10% of the body weight in 6 to 8 seconds. Vectors for hydrodynamic delivery were produced using the Qiagen Plasmid Plus Mega Kit. Equivalent DNA concentration between different batches of DNA was confirmed to ensure reproducibility among experiments. Mice were sacrificed 6 weeks after injection.

IHC and Quantification of Immune Cells

IHC and quantification of immune cells were performed as described previously (80). Primary antibodies used in the IHC staining of mouse liver tumors are listed in Supplementary Table S2. Five microscopic fields (magnification, $\times 200$) of regions of interest were selected and captured. Positively stained cells were counted using Image-Pro Plus (81), and the density of positive cells was calculated by averaging.

Neoantigen Prediction and Depletion

Neoantigens were predicted by NetMHC (v4.0; ref. 82) and NetMHCpan (v4.1; ref. 83) with the following criteria: (i) the length of the peptide was 9 to 10 mer and (ii) minimum IC₅₀ <500 nmol/L in either software. Copy-number loss of clonal neoantigen was detected if the corresponding copy number of the SNV allele was 0. If the read count of the mutation site identified by RNA-seq was more than 5 with at least 3 mutated reads, the neoantigen was defined as expressed neoantigen and otherwise unexpressed as previously described (40). Neoantigens bound to the lost HLA allele were defined as loss of presentation.

Peptide-MHC Tetramer Assay

Peptide-MHC tetramer assays were performed to estimate the affinity between peptide and HLA sites as we previously described (44). Neoantigen peptides were synthesized according to the standard procedure (ABclonal Inc.) with purity >95%. An HLA-A*11:01 tetramer kit (TB-7304-K1, MBL International), an HLA-A*24:02 tetramer kit (TB-7302-K1, MBL International), and an HLA-A*02:01 tetramer kit (TB-7300-K1, MBL International) were used according to the manufacturer's instructions.

Culture and Expansion of T Cells

PBMCs of donors were obtained using Lymphoprep (07851, Stemcell) and then cultured with ImmunoCult-XF T Cell Expansion Medium (10981, Stemcell) and 10 ng/mL human recombinant IL2 (78036, Stemcell). ImmunoCult Human CD3/CD28 T Cell Activator (25 μ L/mL; 10971, Stemcell) was added to the cell suspension and incubated for 3 days. Then the volume of the cell suspension was expanded every 2 days according to the manufacturer's instructions.

ELISpot Assay

ELISpot assays were performed according to the manufacturer's instructions. In brief, we incubated 5×10^4 cells with 10 μ g/mL of the synthesized peptide in each well at 37°C in ELISpot plates (2110003, DAKWE) for 20 hours. The plates were washed and incubated with antihuman IFN γ and then streptavidin-HRP. Finally, the streptavidin-HRP was stained using the AEC solution, and ELISpot plates were scanned and counted using an ImmunoSpot plate reader and associated software (Cellular Technologies, Ltd.).

Coculture of Dendritic Cells and T Cells

The differentiation of monocytes into dendritic cells was conducted using the ImmunoCult Dendritic Cell Culture Kit (10985, Stemcell) according to the manufacturer's instructions. We first obtained PBMCs from a healthy donor and then incubated the cells with a serum-free medium at 37°C for 2 hours. Suspension cells were collected for T-cell expansion, and ImmunoCult dendritic cell differentiation medium with differentiation supplement was added to induce the differentiation of adherent monocytes. The medium was replaced every 2 days. Synthesized peptides were added at 50 μ g/mL and allowed immature dendritic cells to uptake and process on day 5. Maturation supplement was added on day 6 to induce the maturation of dendritic cells. Then mature dendritic cells were obtained on day 8 and cocultured with expanded T cells for 24 hours.

Flow Cytometry

For flow cytometry, antibodies used were anti-CD3 (563800, SK7, BD Biosciences, RRID: AB_2744384), anti-CD8 (557945, RPA-T8, BD Biosciences, RRID: AB_396953), anti-CD107a (328608, H4A3, BioLegend, RRID: AB_1186040), and anti-4-1BB (309804, 4B4-1, BioLegend, RRID: AB_314783). Data were collected using the flow cytometers BD LSRFortessa and Celesta (BD Biosciences), and analyzed by FlowJo (TreeStar).

Peptide Stimulation and 4-1BB⁺ Cell Separation

We incubated 10⁷ cells with 10 µg/mL of peptide #19 or DMSO in 2 mL culture media at 37°C for 24 hours. 4-1BB⁺ cells were obtained using the CD137 MicroBead Kit (130-093-476, Miltenyi Biotec) according to the manufacturer's instructions.

TCR-seq

Genome DNA from peripheral blood, tumor-adjacent tissues, and tumor tissues was collected for TCR-seq. We used the Multiplex PCR (MPCR) primers as described previously (84, 85), which includes 30 forward V primers and 13 reverse J primers, to amplify the rearranged CDR3 regions of TCRs and the sequencing was performed using a BGISEQ-500 platform (MGI Tech Co., Ltd.) following the manufacturer's protocol. Detailed data processing and TCR clonotype detection are described in Supplementary Materials and Methods.

Prognostic Classification System

A simple prognostic classification system was developed based on immune evasion ability for iCCA. Immune infiltration status was determined based on the unsupervised clustering of immune signatures by Danaher and colleagues (27). HLA LOH was called using LOHHLA (86) and CD8⁺ T-cell exhaustion scores were calculated with single-sample gene set enrichment analysis using the signature by Kang and colleagues (62), in which the top 10% of tumor samples were defined as extreme CD8 exhaustion.

Statistical Analysis

Statistical analyses were conducted using SPSS 25.0 software (IBM). The Chi-square test, Fisher exact test, Mann-Whitney *U* test, Kruskal-Wallis test, and Student *t* test were used appropriately. Kaplan-Meier plots (log-rank test) and Cox proportional hazards regression analysis were used to describe survival curves and identify independent prognostic factors, respectively. A two-tailed *P* < 0.05 was considered significant. The results of group comparisons presented as box plots followed these rules: The maximum and minimum are indicated by the extreme points, the median is indicated by the thick horizontal line, and the first and third quartiles are indicated by box edges; whiskers indicate 1.5 times the interquartile range above the first quartile and below the third quartile. The schematic diagrams were drawn using BioRender.

Public Data Sets

Six public data sets were analyzed. We collected multiomics data of the CPTAC iCCA cohort (ref. 19; <https://www.biosino.org/node/project/detail/OEP001105>), somatic mutation data of Zou and colleagues (21) from GeneBank (SRP045202), and the data sets from TCGA. The somatic mutation data of Xiang and colleagues (14), Dong and colleagues (8), and Chen and colleagues (17) were also used to verify our results.

Data Availability

Sequence data have been deposited at the National Omics Data Encyclopedia, which is hosted by the Shanghai Institutes for Biological Sciences, Chinese Academy of Sciences (accession no. OEP002560),

and at CNSA (CNGB Sequence Archive; <https://db.cngb.org/cnsa/>) of the China National GeneBank DataBase (CNGBdb), with the accession code CNP0002045.

Authors' Disclosures

No disclosures were reported.

Authors' Contributions

Y. Lin: Software, formal analysis, validation, methodology, writing—original draft, writing—review and editing. **L. Peng:** Software, formal analysis, investigation, visualization, methodology, writing—original draft, writing—review and editing. **L. Dong:** Software, formal analysis, validation, investigation, methodology, writing—original draft, writing—review and editing. **D. Liu:** Software, formal analysis, validation, investigation, visualization, writing—original draft, writing—review and editing. **J. Ma:** Investigation, methodology, writing—review and editing. **J. Lin:** Validation, investigation, methodology. **X. Chen:** Software, formal analysis, methodology. **P. Liu:** Software, formal analysis, methodology. **G. Song:** Validation, investigation, writing—review and editing. **M. Zhang:** Validation, investigation, methodology, writing—review and editing. **Y. Liu:** Formal analysis, validation, investigation, writing—review and editing. **J. Rao:** Software, formal analysis, methodology. **C. Wei:** Software, formal analysis, writing—review and editing. **Y. Lu:** Software, formal analysis, writing—review and editing. **S. Zhang:** Software, funding acquisition, writing—review and editing. **G. Ding:** Investigation, writing—review and editing. **Z. Peng:** Software, formal analysis, writing—review and editing. **H. Lu:** Software, formal analysis. **X. Wang:** Investigation, writing—review and editing. **J. Zhou:** Investigation, writing—review and editing. **J. Fan:** Conceptualization, resources, supervision, funding acquisition, methodology, writing—original draft, writing—review and editing. **K. Wu:** Conceptualization, resources, supervision, funding acquisition, investigation, writing—original draft, writing—review and editing. **Q. Gao:** Conceptualization, resources, data curation, supervision, funding acquisition, writing—original draft, project administration, writing—review and editing.

Acknowledgments

This study was supported by the National Natural Science Foundation of China (nos. 82130077, 81961128025, and 82002514) to Q. Gao and L. Dong; the Research Projects from the Science and Technology Commission of Shanghai Municipality (grants 21JC1410100, 21JC1401200, 20JC1418900, 19XD1420700, and 20YF1407400) to J. Fan, Q. Gao, S. Zhang, and L. Dong; Guangdong Provincial Key Laboratory of Human Disease Genomics (2020B1212070028) to K. Wu; Science, Technology and Innovation Commission of Shenzhen Municipality under grant JCYJ20170817145208120 to L. Peng; and the China National GeneBank. We thank Mr. Gaoxiang Ge (Chinese Academy of Sciences, Shanghai, China), Mr. Fuqiang Li, Ms. Qing Zhou, and Mr. Chen Ye (BGI-Shenzhen, Shenzhen, China) for their assistance and suggestions on this project.

The costs of publication of this article were defrayed in part by the payment of page charges. This article must therefore be hereby marked *advertisement* in accordance with 18 U.S.C. Section 1734 solely to indicate this fact.

Note

Supplementary data for this article are available at Cancer Discovery Online (<http://cancerdiscovery.aacrjournals.org/>).

Received December 14, 2021; revised May 19, 2022; accepted July 15, 2022; published first July 19, 2022.

REFERENCES

- Sirica AE, Gores GJ, Groopman JD, Selaru FM, Strazzabosco M, Wei Wang X, et al. Intrahepatic cholangiocarcinoma: continuing challenges and translational advances. *Hepatology* 2019;69:1803–15.
- Abou-Alfa GK, Macarulla T, Javle MM, Kelley RK, Lubner SJ, Adeva J, et al. Ivosidenib in IDH1-mutant, chemotherapy-refractory cholangiocarcinoma (ClarIDHy): a multicentre, randomised, double-blind, placebo-controlled, phase 3 study. *Lancet Oncol* 2020;21:796–807.
- Abou-Alfa GK, Sahai V, Hollebecque A, Vaccaro G, Melisi D, Al-Rajabi R, et al. Pemigatinib for previously treated, locally advanced or metastatic cholangiocarcinoma: a multicentre, open-label, phase 2 study. *Lancet Oncol* 2020;21:671–84.
- Cleary JM, Raghavan S, Wu Q, Li YY, Spurr LF, Gupta HV, et al. FGFR2 extracellular domain in-frame deletions are therapeutically targetable genomic alterations that function as oncogenic drivers in cholangiocarcinoma. *Cancer Discov* 2021;11:2488–505.
- Goyal L, Shi L, Liu LY, Fede de la Cruz F, Lennerz JK, Raghavan S, et al. TAS-120 overcomes resistance to ATP-competitive FGFR inhibitors in patients with FGFR2 fusion-positive intrahepatic cholangiocarcinoma. *Cancer Discov* 2019;9:1064–79.
- Kelley RK, Bridgewater J, Gores GJ, Zhu AX. Systemic therapies for intrahepatic cholangiocarcinoma. *J Hepatol* 2020;72:353–63.
- Mittal D, Gubin MM, Schreiber RD, Smyth MJ. New insights into cancer immunoevasion and its three component phases—elimination, equilibrium and escape. *Curr Opin Immunol* 2014;27:16–25.
- Dong LQ, Shi Y, Ma LJ, Yang LX, Wang XY, Zhang S, et al. Spatial and temporal clonal evolution of intrahepatic cholangiocarcinoma. *J Hepatol* 2018;69:89–98.
- Zhang M, Yang H, Wan L, Wang Z, Wang H, Ge C, et al. Single-cell transcriptomic architecture and intercellular crosstalk of human intrahepatic cholangiocarcinoma. *J Hepatol* 2020;73:1118–30.
- Song G, Shi Y, Meng L, Ma J, Huang S, Zhang J, et al. Single-cell transcriptomic analysis suggests two molecularly subtypes of intrahepatic cholangiocarcinoma. *Nat Commun* 2022;13:1642.
- Takahashi M, Lio CJ, Campeau A, Steger M, Ay F, Mann M, et al. The tumor suppressor kinase DAPK3 drives tumor-intrinsic immunity through the STING-IFN- β pathway. *Nat Immunol* 2021;22:485–96.
- Braun DA, Street K, Burke KP, Cookmeyer DL, Denize T, Pedersen CB, et al. Progressive immune dysfunction with advancing disease stage in renal cell carcinoma. *Cancer Cell* 2021;39:632–48.
- Wu Y, Yang S, Ma J, Chen Z, Song G, Rao D, et al. Spatiotemporal immune landscape of colorectal cancer liver metastasis at single-cell level. *Cancer Discov* 2022;12:134–53.
- Xiang X, Liu Z, Zhang C, Li Z, Gao J, Zhang C, et al. IDH mutation subgroup status associates with intratumor heterogeneity and the tumor microenvironment in intrahepatic cholangiocarcinoma. *Adv Sci* 2021;8:e2101230.
- Valle JW, Lamarca A, Goyal L, Barriuso J, Zhu AX. New horizons for precision medicine in biliary tract cancers. *Cancer Discov* 2017;7:943–62.
- Artegiani B, van Voorthuisen L, Lindeboom RG, Seinstra D, Heo I, Tapia P, et al. Probing the tumor suppressor function of BAP1 in CRISPR-engineered human liver organoids. *Cell Stem Cell* 2019;24:927–43.
- Chen S, Xie Y, Cai Y, Hu H, He M, Liu L, et al. Multiomic analysis reveals comprehensive tumor heterogeneity and distinct immune subtypes in multifocal intrahepatic cholangiocarcinoma. *Clin Cancer Res* 2022;28:1896–910.
- Shen J, Ju Z, Zhao W, Wang L, Peng Y, Ge Z, et al. ARID1A deficiency promotes mutability and potentiates therapeutic antitumor immunity unleashed by immune checkpoint blockade. *Nat Med* 2018;24:556–62.
- Dong L, Lu D, Chen R, Lin Y, Zhu H, Zhang Z, et al. Proteogenomic characterization identifies clinically relevant subgroups of intrahepatic cholangiocarcinoma. *Cancer Cell* 2022;40:70–87.
- Farshidfar F, Zheng S, Gingras MC, Newton Y, Shih J, Robertson AG, et al. Integrative genomic analysis of cholangiocarcinoma identifies distinct IDH-mutant molecular profiles. *Cell Rep* 2017;18:2780–94.
- Zou S, Li J, Zhou H, Frech C, Jiang X, Chu JS, et al. Mutational landscape of intrahepatic cholangiocarcinoma. *Nat Commun* 2014;5:5696.
- Canon J, Rex K, Saiki AY, Mohr C, Cooke K, Bagal D, et al. The clinical KRAS(G12C) inhibitor AMG 510 drives anti-tumour immunity. *Nature* 2019;575:217–23.
- Nagasaka M, Li Y, Sukari A, Ou SI, Al-Hallak MN, Azmi AS. KRAS G12C Game of Thrones, which direct KRAS inhibitor will claim the iron throne? *Cancer Treat Rev* 2020;84:101974.
- Uprety D, Adjei AA. KRAS: From undruggable to a druggable cancer target. *Cancer Treat Rev* 2020;89:102070.
- André F, Ciruelos EM, Juric D, Loibl S, Campone M, Mayer IA, et al. Alpelisib plus fulvestrant for PIK3CA-mutated, hormone receptor-positive, human epidermal growth factor receptor-2-negative advanced breast cancer: final overall survival results from SOLAR-1. *Ann Oncol* 2021;32:208–17.
- de Bono J, Mateo J, Fizazi K, Saad F, Shore N, Sandhu S, et al. Olaparib for metastatic castration-resistant prostate cancer. *N Engl J Med* 2020;382:2091–102.
- Danaher P, Warren S, Dennis L, D'Amico L, White A, Disis ML, et al. Gene expression markers of tumor-infiltrating leukocytes. *J Immunother Cancer* 2017;5:18.
- Rooney MS, Shukla SA, Wu CJ, Getz G, Hacohen N. Molecular and genetic properties of tumors associated with local immune cytolytic activity. *Cell* 2015;160:48–61.
- Ayers M, Lunceford J, Nebozhyn M, Murphy E, Loboda A, Kaufman DR, et al. IFN- γ -related mRNA profile predicts clinical response to PD-1 blockade. *J Clin Invest* 2017;127:2930–40.
- Hammerl D, Martens JWM, Timmermans M, Smid M, Trapman-Jansen AM, Foekens R, et al. Spatial immunophenotypes predict response to anti-PD-1 treatment and capture distinct paths of T cell evasion in triple-negative breast cancer. *Nat Commun* 2021;12:5668.
- Sia D, Jiao Y, Martinez-Quetglas I, Kuchuk O, Villacorta-Martin C, Castro de Moura M, et al. Identification of an immune-specific class of hepatocellular carcinoma, based on molecular features. *Gastroenterology* 2017;153:812–26.
- Chen YP, Wang YQ, Lv JW, Li YQ, Chua MLK, Le QT, et al. Identification and validation of novel microenvironment-based immune molecular subgroups of head and neck squamous cell carcinoma: implications for immunotherapy. *Ann Oncol* 2019;30:68–75.
- Xiao Y, Ma D, Zhao S, Suo C, Shi J, Xue MZ, et al. Multi-omics profiling reveals distinct microenvironment characterization and suggests immune escape mechanisms of triple-negative breast cancer. *Clin Cancer Res* 2019;25:5002–14.
- Liberzon A, Birger C, Thorvaldsdóttir H, Ghandi M, Mesirov JP, Tamayo P. The Molecular Signatures Database (MSigDB) hallmark gene set collection. *Cell Syst* 2015;1:417–25.
- Bezzi M, Seitzer N, Ishikawa T, Reschke M, Chen M, Wang G, et al. Diverse genetic-driven immune landscapes dictate tumor progression through distinct mechanisms. *Nat Med* 2018;24:165–75.
- Liu H, Liang Z, Zhou C, Zeng Z, Wang F, Hu T, et al. Mutant KRAS triggers functional reprogramming of tumor-associated macrophages in colorectal cancer. *Signal Transduct Target Ther* 2021;6:144.
- Shang A, Gu C, Zhou C, Yang Y, Chen C, Zeng B, et al. Exosomal KRAS mutation promotes the formation of tumor-associated neutrophil extracellular traps and causes deterioration of colorectal cancer by inducing IL-8 expression. *Cell Commun Signal* 2020;18:52.
- Wu MJ, Shi L, Dubrot J, Merritt J, Vijay V, Wei TY, et al. Mutant IDH inhibits IFN γ -TET2 signaling to promote immune evasion and tumor maintenance in cholangiocarcinoma. *Cancer Discov* 2022;12:812–35.
- Arzumanyan A, Reis HM, Feitelson MA. Pathogenic mechanisms in HBV- and HCV-associated hepatocellular carcinoma. *Nat Rev Cancer* 2013;13:123–35.
- Rosenthal R, Cadieux EL, Salgado R, Bakir MA, Moore DA, Hiley CT, et al. Neoantigen-directed immune escape in lung cancer evolution. *Nature* 2019;567:479–85.
- Jones PA, Ohtani H, Chakravarthy A, De Carvalho DD. Epigenetic therapy in immune-oncology. *Nat Rev Cancer* 2019;19:151–61.

42. McGranahan N, Swanton C. Clonal heterogeneity and tumor evolution: past, present, and the future. *Cell* 2017;168:613–28.
43. Reuben A, Gittelman R, Gao J, Zhang J, Yusko EC, Wu CJ, et al. TCR repertoire intratumor heterogeneity in localized lung adenocarcinomas: an association with predicted neoantigen heterogeneity and postsurgical recurrence. *Cancer Discov* 2017;7:1088–97.
44. Dong LQ, Peng LH, Ma LJ, Liu DB, Zhang S, Luo SZ, et al. Heterogeneous immunogenomic features and distinct escape mechanisms in multifocal hepatocellular carcinoma. *J Hepatol* 2020;72:896–908.
45. Liu Y, Zhang Q, Xing B, Luo N, Gao R, Yu K, et al. Immune phenotypic linkage between colorectal cancer and liver metastasis. *Cancer Cell* 2022;40:424–37.
46. Hsueh EH, Wright KM, Douglass J, Hwang MS, Mog BJ, Pearlman AH, et al. Targeting a neoantigen derived from a common TP53 mutation. *Science* 2021;371:eabc8697.
47. Sim MJW, Lu J, Spencer M, Hopkins F, Tran E, Rosenberg SA, et al. High-affinity oligoclonal TCRs define effective adoptive T cell therapy targeting mutant KRAS-G12D. *Proc Natl Acad Sci U S A* 2020;117:12826–35.
48. Tran E, Robbins PF, Lu YC, Prickett TD, Gartner JJ, Jia L, et al. T-cell transfer therapy targeting mutant KRAS in cancer. *N Engl J Med* 2016;375:2255–62.
49. Hilligan KL, Ronchese F. Antigen presentation by dendritic cells and their instruction of CD4⁺ T helper cell responses. *Cell Mol Immunol* 2020;17:587–99.
50. Glanville J, Huang H, Nau A, Hatton O, Wagar LE, Rubelt F, et al. Identifying specificity groups in the T cell receptor repertoire. *Nature* 2017;547:94–8.
51. Palakurthi S, Kuraguchi M, Zacharek SJ, Zudaire E, Huang W, Bonal DM, et al. The combined effect of FGFR inhibition and PD-1 blockade promotes tumor-intrinsic induction of antitumor immunity. *Cancer Immunol Res* 2019;7:1457–71.
52. Huang YH, Zhang CZ, Huang QS, Yeong J, Wang F, Yang X, et al. Clinicopathologic features, tumor immune microenvironment and genomic landscape of Epstein–Barr virus-associated intrahepatic cholangiocarcinoma. *J Hepatol* 2021;74:838–49.
53. Nejo T, Matsushita H, Karasaki T, Nomura M, Saito K, Tanaka S, et al. Reduced neoantigen expression revealed by longitudinal multomics as a possible immune evasion mechanism in glioma. *Cancer Immunol Res* 2019;7:1148–61.
54. Angelova M, Mlecnik B, Vasaturo A, Bindea G, Fredriksen T, Lafontaine L, et al. Evolution of metastases in space and time under immune selection. *Cell* 2018;175:751–65.
55. Anagnostou V, Smith KN, Forde PM, Niknafs N, Bhattacharya R, White J, et al. Evolution of neoantigen landscape during immune checkpoint blockade in non-small cell lung cancer. *Cancer Discov* 2017;7:264–76.
56. Grasso CS, Giannakis M, Wells DK, Hamada T, Mu XJ, Quist M, et al. Genetic mechanisms of immune evasion in colorectal cancer. *Cancer Discov* 2018;8:730–49.
57. Zaravinos A, Roufas C, Nagara M, de LMoreno B, Oblovatskaya M, et al. Cytolytic activity correlates with the mutational burden and deregulated expression of immune checkpoints in colorectal cancer. *J Exp Clin Cancer Res* 2019;38:364.
58. Jusakul A, Cutcutache I, Yong CH, Lim JQ, Huang MN, Padmanabhan N, et al. Whole-genome and epigenomic landscapes of etiologically distinct subtypes of cholangiocarcinoma. *Cancer Discov* 2017;7:1116–35.
59. Hinshaw DC, Shevde LA. The tumor microenvironment innately modulates cancer progression. *Cancer Res* 2019;79:4557–66.
60. Zhou G, Sprengers D, Mancham S, Erkens R, Boor PPC, van Beek AA, et al. Reduction of immunosuppressive tumor microenvironment in cholangiocarcinoma by ex vivo targeting immune checkpoint molecules. *J Hepatol* 2019;71:753–62.
61. Jia Q, Wu W, Wang Y, Alexander PB, Sun C, Gong Z, et al. Local mutational diversity drives intratumoral immune heterogeneity in non-small cell lung cancer. *Nat Commun* 2018;9:5361.
62. Kang HJ, Oh JH, Chun SM, Kim D, Ryu YM, Hwang HS, et al. Immunogenomic landscape of hepatocellular carcinoma with immune cell stroma and EBV-positive tumor-infiltrating lymphocytes. *J Hepatol* 2019;71:91–103.
63. Peng Q, Qiu X, Zhang Z, Zhang S, Zhang Y, Liang Y, et al. PD-L1 on dendritic cells attenuates T cell activation and regulates response to immune checkpoint blockade. *Nat Commun* 2020;11:4835.
64. Hartley GP, Chow L, Ammons DT, Wheat WH, Dow SW. Programmed cell death ligand 1 (PD-L1) signaling regulates macrophage proliferation and activation. *Cancer Immunol Res* 2018;6:1260–73.
65. Affo S, Nair A, Brundu F, Ravichandra A, Bhattacharjee S, Matsuda M, et al. Promotion of cholangiocarcinoma growth by diverse cancer-associated fibroblast subpopulations. *Cancer Cell* 2021;39:866–82.
66. Kadam P, Sharma S. PD-1 immune checkpoint blockade promotes therapeutic cancer vaccine to eradicate lung cancer. *Vaccines* 2020;8:317.
67. Kadam P, Singh RP, Davoodi M, Lee JM, John MS, Sharma S. Immune checkpoint blockade enhances immune activity of therapeutic lung cancer vaccine. *Vaccines* 2020;8:655.
68. Ott PA, Hu Z, Keskin DB, Shukla SA, Sun J, Bozym DJ, et al. An immunogenic personal neoantigen vaccine for patients with melanoma. *Nature* 2017;547:217–21.
69. Getts D, Hofmeister R, Quintás-Cardama A. Synthetic T cell receptor-based lymphocytes for cancer therapy. *Adv Drug Deliv Rev* 2019;141:47–54.
70. Shi JY, Gao Q, Wang ZC, Zhou J, Wang XY, Min ZH, et al. Margin-infiltrating CD20(+) B cells display an atypical memory phenotype and correlate with favorable prognosis in hepatocellular carcinoma. *Clin Cancer Res* 2013;19:5994–6005.
71. Job S, Rapoud D, Dos Santos A, Gonzalez P, Desterke C, Pascal G, et al. Identification of four immune subtypes characterized by distinct composition and functions of tumor microenvironment in intrahepatic cholangiocarcinoma. *Hepatology* 2019;72:965–81.
72. Davoli T, Uno H, Wooten EC, Elledge SJ. Tumor aneuploidy correlates with markers of immune evasion and with reduced response to immunotherapy. *Science* 2017;355:eaaf8399.
73. Racle J, de Jonge K, Baumgaertner P, Speiser DE, Gfeller D. Simultaneous enumeration of cancer and immune cell types from bulk tumor gene expression data. *eLife* 2017;6:e26476.
74. Li B, Severson E, Pignoni JC, Zhao H, Li T, Novak J, et al. Comprehensive analyses of tumor immunity: implications for cancer immunotherapy. *Genome Biol* 2016;17:174.
75. Shen YC, Hsu CL, Jeng YM, Ho MC, Ho CM, Yeh CP, et al. Reliability of a single-region sample to evaluate tumor immune microenvironment in hepatocellular carcinoma. *J Hepatol* 2020;72:489–97.
76. Charoentong P, Finotello F, Angelova M, Mayer C, Efremova M, Rieder D, et al. Pan-cancer immunogenomic analyses reveal genotype-immunophenotype relationships and predictors of response to checkpoint blockade. *Cell Rep* 2017;18:248–62.
77. Bindea G, Mlecnik B, Tosolini M, Kirilovsky A, Waldner M, Obenauf AC, et al. Spatiotemporal dynamics of intratumoral immune cells reveal the immune landscape in human cancer. *Immunity* 2013;39:782–95.
78. Hendry S, Salgado R, Gevaert T, Russell PA, John T, Thapa B, et al. Assessing tumor-infiltrating lymphocytes in solid tumors: a practical review for pathologists and proposal for a standardized method from the International Immuno-Oncology Biomarkers Working Group: Part 2: TILs in melanoma, gastrointestinal tract carcinomas, non-small cell lung carcinoma and mesothelioma, endometrial and ovarian carcinomas, squamous cell carcinoma of the head and neck, genitourinary carcinomas, and primary brain tumors. *Adv Anat Pathol* 2017;24:311–35.
79. Ma LJ, Feng FL, Dong LQ, Zhang Z, Duan M, Liu LZ, et al. Clinical significance of PD-1/PD-Ls gene amplification and overexpression in patients with hepatocellular carcinoma. *Theranostics* 2018;8:5690–702.
80. Zheng BH, Ma JQ, Tian LY, Dong LQ, Song GH, Pan JM, et al. The distribution of immune cells within combined hepatocellular carcinoma and cholangiocarcinoma predicts clinical outcome. *Clin Transl Med* 2020;10:45–56.
81. Ahn H, Lee HJ, Lee JH, Cho HD, Oh MH, Son JW, et al. Clinicopathological correlation of PD-L1 and TET1 expression with

- tumor-infiltrating lymphocytes in non-small cell lung cancer. *Pathol Res Pract* 2020;216:153188.
82. Andreatta M, Nielsen M. Gapped sequence alignment using artificial neural networks: application to the MHC class I system. *Bioinformatics* 2016;32:511–7.
 83. Reynisson B, Alvarez B, Paul S, Peters B, Nielsen M. NetMHCpan-4.1 and NetMHCIpan-4.0: improved predictions of MHC antigen presentation by concurrent motif deconvolution and integration of MS MHC eluted ligand data. *Nucleic Acids Res* 2020;48:W449–W54.
 84. Zhang W, Du Y, Su Z, Wang C, Zeng X, Zhang R, et al. IMonitor: a robust pipeline for TCR and BCR repertoire analysis. *Genetics* 2015; 201:459–72.
 85. Liu X, Zhang W, Zeng X, Zhang R, Du Y, Hong X, et al. Systematic comparative evaluation of methods for investigating the TCR β repertoire. *PLoS One* 2016;11:e0152464.
 86. McGranahan N, Rosenthal R, Hiley CT, Rowan AJ, Watkins TBK, Wilson GA, et al. Allele-specific HLA loss and immune escape in lung cancer evolution. *Cell* 2017;171:1259–71.